Ph.D. Dissertation of Engineering

Interfacial modification tailored by degradation of Ni-rich layered oxide for Li-ion batteries

리튬이온 전지용 고-니켈계 층상형 양극재의 퇴화 거동 기반 맞춤형 계면 개질

2023년 2월

서울대학교 대학원
화학생물공학부
정 성 훈

Interfacial modification tailored by degradation of Ni-rich layered oxide for Li-ion batteries

Advisor Kyu Tae Lee

Submitting a Ph.D. Dissertation of engineering

February 2023

Graduate School of Engineering
Seoul National University
Chemical and Biological Engineering

Seonghun Jeong

Confirming the Ph.D. Dissertation written by
Seonghun Jeong
February 2023

Chair	Lee, Won Bo	(Seal)
Vice Chair	Lee, Kyu Tae	(Seal)
Examiner	Ryu, Ji Heon	(Seal)
Examiner	Mun, Junyoung	(Seal)
Examiner	Kim, Youngjin	(Seal)

Abstract

Ni-rich layered oxides with the formula of $LiNi_xCo_yMn_zO_2$ ($x > 0.8$, $x+y+z = 1$) is the top candidates for positive materials for high energy density Lithium-ion batteries (LIB) because of their affordable cost and high capacity. However, despite the advantages of Ni-rich layered oxides, several hurdles to the application of these materials are reported. Ni-rich layered oxide has an unstable surface with significant lithium impurities and the unstable surface of Ni-rich layered oxide release lithium impurities when it encounters with water. The Ni ion in a Ni-rich layered oxide is oxide to unstable Ni^{4+}, inducing the transition to a stable rock-salt phase with oxygen evolution. The degradation is severe at the surface because the oxidative decomposition provides electrons which are necessary for the reduction. Various surface modification methods have been proposed to mitigate the surface side reactions. The impurities cause not only safety problems but homogenous inhomogeneity in electrode manufacturing. Therefore, the interfacial modification using an aqueous solution is considered to remove impurities and increase the stability of the surface at the same time. However, the washing

process induces the degradation of the cathode materials. Ni-rich layered oxide suffers from the large anisotropic volume change during cycling, leading the microcrack failure. In terms that the grain boundary modification mitigating microcrack, the internal side reaction is a critical issue.

Herein, the Li^+/H^+ ion exchange and NiO like phase during the washing and subsequent drying process are investigated. NiO like phase leads to the degradation of Ni-rich layered oxide. To eliminate the problematic phase, interfacial modification with Li_2MnO_3 is conducted. It is discovered that the calcination of 800°C induces the Ni doping in Li_2MnO_3 by the delithiation at 4.65 V vs. Li/Li^+. The Ni-doped Li_2MnO_3 surface layer is effective in consuming NiO like phase and stabilizing the surface. As a result, the cathode material with Ni-doped Li_2MnO_3 exhibits improved capacity retention of 88.3% at the 100th cycle and a high rate capability of 76.9% at a current density of 5C compared to a current density of 0.2C.

To prevent electrolyte penetration into a secondary particle, the electrolyte-phobic coating is established using octyltrichlorosilane (OTS), which is one of a self-assembled molecular monolayer (SAM). A homogeneous single layer is delivered on the surface of Ni-rich layered oxide owing to the self-terminating of SAM. The electrolyte-phobic property is effective for mitigating the

propagation of microcracks by reducing the generation of the gas phase from the electrolyte decomposition.

Keyword : Lithium ion batteries, Ni-rich layered oxide, interfacial modification, self-assembled monolayer, washing, microcrack

Student Number : 2019-34401

Table of Contents

List of figures

List of tables

1. Introduction

Global warming shifts the paradigm of rechargeable batteries to large-scale applications such as electric vehicles and energy storage systems.[1-4] Lithium-ion batteries (LIBs) are considered the best candidate among rechargeable battery systems owing to their high energy density. However, despite the relatively high energy density of LIBs, the current energy density of LIBs is still insufficient.[5-7] Therefore, the development of LIBs having higher energy density than the current level is demanded. The best approach to increase energy density is applying high-capacity materials. For anode materials, various types of materials have been proposed.[8-13] However, candidates for high energy density cathode materials are limited owing to their complex crystalline structure.

$LiCoO_2$, which is the conventional cathode material, has a theoretical capacity of 274 mAh g^{-1}.[14-16] However, when more than half of the lithium ions in the structure are extracted, an irreversible phase transition occurs, so the practical capacity is limited to 140 mAh g^{-1}.[15, 17] Various studies have been attempted for increasing the energy density of cathode. Among them, NCM ternary cathode materials in which expensive cobalt ions are substituted with nickel or manganese ions have been studied.[18-22] Especially, Ni-rich cathode materials

with the chemical formula $LiNi_xCo_yMn_zO_2$ ($x+y+z = 1$, $x > 0.8$) are considered the top candidate for high energy density LIBs because they have a practical capacity of over 200 mAh g^{-1}.[23-26]

Despite the advantage of Ni-rich layered oxides, they have several obstacles to application. First, the instability of Ni ions causes a significant intensification of the surface side reaction. Ni ions are oxidized to unstable Ni^{4+} during the charging process. Since the Ni^{4+} ion orbital overlaps with the oxygen 2p orbital, the oxygen molecule is easily extracted from the structure, forming the NiO phase.[27, 28] Meanwhile, when the electron energy density of the electrode is lower than the highest energy molecular orbital (HOMO) level of the electrolyte, oxidative decomposition of the electrolyte occurs to form solid electrolyte interfaces (SEIs).[29-32] Since the electrons generated in this process are used for Ni ion reduction, the cathode material deteriorates severely at the interface in contact with the electrolyte. To alleviate surface side reactions, research on surface modification has been conducted.[33-38]

Second, the unavoidable residual impurities of Ni-rich cathode materials cause detrimental problems. Ni^{2+} ions (0.69 Å) have similar ion sizes to lithium ions (0.76 Å), and Ni^{2+} ions are more stable than Ni^{3+} ions. These cause Ni ions to migrate into the Li layer of the structure to form a non-stoichiometric Li-deficient products.[39-41] Ni

ions in the lithium−ion layer impede the diffusion of lithium ions. Excess lithium is required to alleviate this phenomenon. As a result, the unreacted lithium precursors remain on the surface as impurities such as Li_2CO_3 and LiOH.[18] The impurities increase with increasing the Ni ion contents in transition metal. In addition, when Ni−rich layered oxide powders encounter moisture, the lithium ions are released from the structure, forming lithium impurities.[42−44] Therefore, they should be stored in an inert atmosphere. The impurities are electrochemical decomposed during the charging process, which generates molecules such as CO_2 and O_2, deteriorating the batteries by swelling.[45, 46] In addition, LiOH reacts with PF_6^-, generating harmful fluoric acid,[47, 48] which attacks the SEI and active materials. The basic impurities cause the dehydrofluorination of polyvinyl difluoride (PVdF) binder, triggering the gelation of the slurry.[49] The aggregated slurry state is a challenging issue for the mass production of LIBs. To reduce lithium impurities, the most facile method is the aqueous washing of Ni−rich layered oxide powder.[50−52] Because a significant amount of lithium impurities can be removed with an inexpensive aqueous solution, washing with water is economical in the manufacturing process. However, the washing promotes the intercalation of H^+ ions in the Li^+ ion site, leading to the formation of NiO like phase.[50, 51] This phase

is electrochemically inactive. Therefore, the electrochemical performance worsens after washing.

Third, Ni-rich layered oxide suffers from a unique failure mode of microcrack resulting from the high-volume change during the reaction. The simple layered oxide, $LiCoO_2$ is synthesized using a solid-state mix and high-temperature calcination. Unlike $LCoO_2$, NCM ternary cathode materials should be obtained by co-precipitation-assisted solid-state reaction for uniform transition metal distributions. As a result, several micrometers of secondary particles scale with aggregated primary particles in the nanometer scale are synthesized.[53, 54] Although the a-axis lattice changes similarly even if the nickel content is altered, the changes in the c-axis lattice are severe as the nickel content increases.[55] Thus, anisotropic volume change takes place for Ni-rich layered oxide. The different morphology and high-volume change cause a unique failure mode. Microcrack causes the side reaction on the new interface and inhibition of electron transport. Although many studies have revealed that the anisotropic volume change is the origin of the microcrack,[56, 57] in terms of electrolyte penetration along with grain boundary, an internal side reaction can be a possible reason. Similarly, an approach that grain boundaries was modified to alleviate electrolyte decomposition inside particles has also been attempted to solve the

microcrack failure.[58-61]

We investigated the surface degradation of Ni-rich layered oxide caused by washing using an aqueous solvent. It was demonstrated that Li ions in the structure were exchanged with H^+ ions during washing. As a result, proton exchanged NiOOH was formed. The phase was decomposed to a harmful NiO like phase during the drying process. To eliminate NiO like phase and lithium impurities, an interfacial modification with Ni-doped Li_2MnO_3 was applied. A simple washing process in manganese sulfate solution and subsequent calcination were performed to incorporate Ni ions from NiO like phase into Li_2MnO_3. It is found that the self-precipitated Mn precursor reacted with the remained lithium impurities, forming Li_2MnO_3, which is stable in the voltage range where the Ni-rich layered oxide operates. Ni doping in the Li_2MnO_3 phase was confirmed through an electrochemical reaction at 4.65 V as well as X-ray photoelectron spectroscopy (XPS), scanning transmission electron microscopy (STEM), and time-of-flight secondary ion mass spectroscopy (ToF-SIMS) analyses. The Ni-rich layered oxide modified with Ni-doped Li_2MnO_3 layer had improved electrochemical performance.

SAM is a versatile molecular-level thin coating technique that is homogeneously prepared via spontaneous chemical reactions due to

self-terminates after single layer deposition.[62-64] Additionally, the characteristics of SAM can be finely tuned by controlling the molecular structure of the coupling agent.[63, 64] To deliver an electrolyte-phobic surface modification, octyltrichlorosilane (OTS), one of the most credible ones among the various SAMs examined, is used.[65-67] Vapor deposition is applied to eliminate the solvent issue. It is demonstrated that the electrolyte-phobic coating from the OTS successfully alleviates the electrolyte penetration along with grain boundaries and the internal side reaction with the propagation of the microcracks.

2. Background

2.1. Electrochemical reaction

An electrochemical reaction is a chemical reaction which is dealt with the relation between electrical energy and chemical change. Reactants are oxidized or reduced because electrons, which are considered chemical species, such as ions or elements, participate in the reaction. A cathode is an electrode in which the reduction reaction occurs, and an anode is an electrode in which the oxidation reaction occurs. For electrochemical reactions, electron transport is required between the electrode and reactant. Electrons transport is possible by the tunneling effect due to the wave property of the electron. Therefore, an electron can move between the electrode and the reactant. As a result, the reactant is oxidized or reduced. The electron transfer is only possible when the electrode and reactant are close because the tunneling rate exponentially decreases as the distance between the electrode and the reactant increases. Therefore, mass transfer of the reactant is required for the electrochemical reaction because the reactant located far from the electrode, that can exchange electrons, can participate in the electrochemical reaction

only when it approaches the electrode.

The electrical energy generated from the battery during discharge is determined by the electrochemical reaction of the system. If the following electrochemical reaction takes place at the electrode,

$$aA + bB \rightarrow cC + dD$$

where, a, b, c, and d mean stoichiometric coefficients for each species of A, B, C and D. The Gibbs free energy change in the above reaction can be expressed as follows.

$$\Delta G = \Delta G^o + RT \ln \left(\frac{a_C^c a_D^d}{a_A^a a_B^b}\right)$$

Meanwhile, the work (W_{rev}), which can be obtained from a battery at equilibrium, is equal to the maximum work (W_{max}), which is expressed as a change in Gibbs free energy change during an electrochemical reaction, it can be expressed as below.

$$W_{rev} = W_{max}$$

$$-W_{max} = \Delta G$$

Meanwhile, electrical energy can be expressed as follows the electric charge (Q) and the potential difference (E) flowing inside the battery.

$$-W_{max} = Q\,E$$

where, Q is represented by the multiple of the total electron number and the charge of one electron, and the number of electrons. n_e is the multiple of the Avogadro number and mole of the electron. Q is expressed below through the mole of electron (n) and the charge of the electron.

$$Q = n_e\,e$$

$$Q = n\,N_A\,e$$

Also, charge Q is represented by F, which is the charge of one mole of the electron.

$$Q = n\,F$$

where, F is Faraday constant, 96485 C/ mol. Based on this, when the two electrodes have different potentials and n moles of electrons move due to the potential difference, the electrical work

corresponding to the battery is expressed by the following formula.

$$W_{max} = n\,F\,E$$

$$-\Delta G = n\,F\,E$$

This equation shows the relationship between the electromotive force and the change in Gibbs free energy that we can obtain from the cell in the equilibrium state through the electrochemical reaction. In the case of all the reactants and products participating in the electrochemical reaction are in the standard state, that is, at a t of 0°C and pressure of 1 atm, the potential of the cell is expressed as the standard potential, E^o.

$$-\Delta G^o = n\,F\,E^o$$

Therefore, if ΔG < 0, the reaction is a spontaneous and the potential difference (E) of the cell > 0 as the case of a discharge process that obtains energy from a battery. Conversely, if ΔG > 0, it is an unspontaneous reaction, and the potential difference of the cell < 0 as the charging process that requires an external energy supply.

2.2. Secondary battery system

Secondary batteries are mainly composed of a positive electrode with a relatively high oxidation/reduction reaction potential, a negative electrode with a relatively low reaction potential, an electrolyte, and a separator. The role of an electrolyte is a carrier of ions between the two electrodes, and a separator prevents direct contact between the two electrodes. A positive electrode and negative electrode are fabricated by casting the slurry on an aluminum foil as a positive electrode current collector or a copper foil as a negative electrode current collector. The slurry is prepared by combining active material capable of electrochemically reacting with active ions, a conducting agent for increasing electrical conductivity, and a binder for adhesion between the active material. In a lithium-ion secondary battery system, lithium ions are extracted from the cathode structure and move to the electrolyte during the charging process as shown in **Figure 1a**. In this process, the potential of the cathode increases. On the other hand, in the negative electrode, lithium-ion in the electrolyte reacts with the negative electrode, decreasing the potential of the negative electrode. Finally, the voltage of the cell, which is the potential difference between the anode and the cathode, rises. Conversely, in the discharge process, lithium ions

are de-litigated from the lithiated negative electrode and move to the electrolyte as shown in **Figure 1b**, increasing the potential of the anode. Therefore, the voltage of the cell is down. In the secondary battery system, an oxidation reaction occurs during the charging process and a reduction reaction occurs during the discharging process in the positive electrode. On the other hand, a reduction reaction occurs during a charging process and an oxidation reaction occurs during the discharging process in the negative electrode. Therefore, since the distinction between the cathode and the anode is not clear, a positive electrode in which a reduction reaction occurs is considered a cathode and a negative electrode where an oxidation reaction takes place is considered an anode based on the discharge process.

In battery systems, polarization refers to a phenomenon in which an electrode potential value becomes excessive or insufficient in an equilibrium state. Because the transfers of charge generated in each component of the battery are different, the slowest reaction is defined as a rate-limiting process for the entire reaction. The overall reaction rate depends on the rate-limiting process. Therefore, when a current flows between both electrodes of the battery, the voltage, E measured between both electrodes is always greater or less than the equilibrium voltage (E_{eq}, equilibrium potential). The difference

between the measured voltage and the equilibrium voltage between the two electrodes is overpotential. It is a method of measuring the actual degree of polarization. That is, the relationship between the measured voltage (E), the equilibrium voltage (E_{eq}), and the overvoltage (η) is as follows.

$$\eta = E - E_{eq}$$

Here, the polarization is divided into three main categories: ohmic polarization caused by iR drop, activation polarization mainly due to electrode characteristics, and concentration polarization. The iR drop is a characteristic due to the internal resistance of the cell. In particular, to prevent a significant operating voltage drop when the high current density is applied, the internal resistance should be minimized, since the iR drop increases in proportion to the current density like ohmic's law. The internal resistance contains the solution resistance that is a reciprocal of ionic conductivity. On the other hand, activation polarization is closely related to the characteristics of the electrode, which is a fundamental factor according to the type of active material and is greatly affected by temperature. In addition, the polarization expressed by the concentration gradient of the reactant on the surface is classified as concentration polarization.

However, these elements appear to be combined, making it difficult to distinguish them as shown in **Figure 2**.

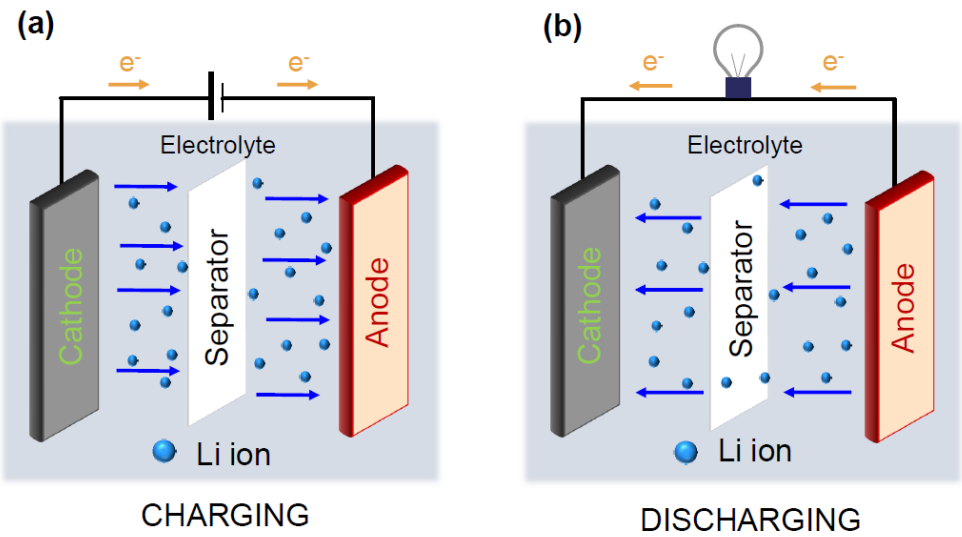

Figure 1. The movements of Li-ion and electrons in lithium-ion batteries during the (a) charging and (b) discharging.

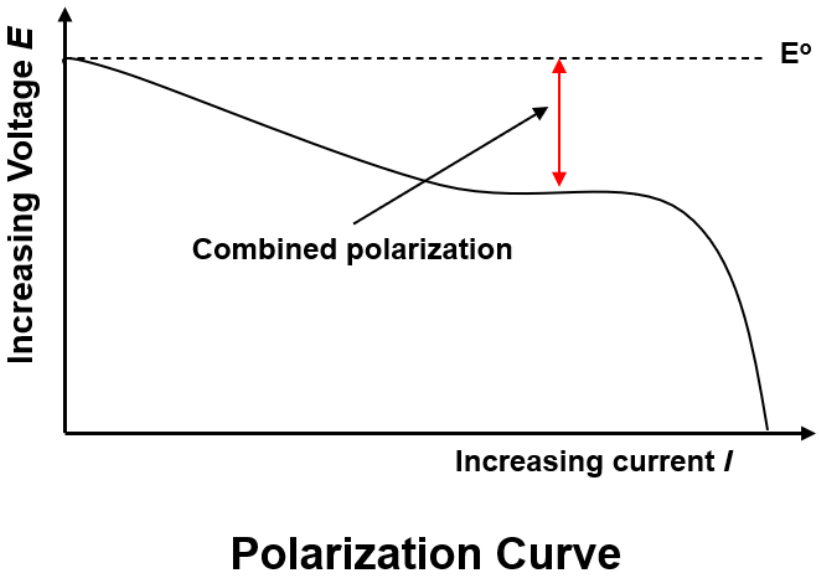

Figure 2. The polarization curve depending on the current.

2.3. Cathode materials

2.3.1. Layered structure cathodes

In the case of a cathode material, it should react with lithium ions reversibly without the structure change during charging/discharging. According to this, studies on the layered structure in which lithium ions are intercalated/deintercalated reversibly were conducted. As a result, it was found that lithium-ion interacts in a layered structure such as TiS_2. However, this material failed to commercialize due to high raw material costs and a complicated synthesis process. After that, MoS_2 positive electrode material was developed, and secondary battery using MoS_2 as positive electrode and Li metal as negative electrode was developed. However, dendrite grows during continuous charging/discharge, which induces an internal short circuit, and hindered commercialization. Due to these results, research on anode materials using carbon instead of Li metal has been started. Unlike lithium metal, the carbon-based anode materials do not contain Li ions, so the cathode material must contain lithium-ions. In addition, since the reaction voltage is not relatively high in the case of transition metal sulfide, a cathode material made of oxide with a relatively high reaction voltage has received attention, and

research on cathode materials such as $LiMeO_2$ (Me is transition metal ions) has finally begun. The chemical formula of $LiMeO_2$ has a layered structure through ionic bonding. The densest structure composed of oxygen ions, lithium ions, and transition metal ions can be formed by preferentially forming a dense structure with oxygen ions having the largest ionic radius among the three ions. Next, lithium ions and transition metal ions are located at the interstitial site on the constructed oxygen ions. The oxygen ion layer is located at the cubic closed packed structure. Tetrahedral and octahedral interstitial sites exist between the oxygen ions. Cations occupies the empty sites. As the number of bonds between cations and anions increases, they become relatively stable, so cations prefer an octahedral site with a high coordination number. In addition, if there are n oxygen atoms in the cubic structure, 2n tetrahedral sites and n octahedral sites exist. Also, If the ratio of transition metal ion radius (r) to oxygen ion radius (R) (r/R) is 0.225 to 0.414, cations occupy a tetrahedral site, and if the ratio is 0.414 to 0.732, they occupy octahedral sites. In general, since the ionic radius ratio between 3d transition metal ions and oxygen ions $r(Me^{3+})/R(O^{2-})$ is 0.5397 to 0.7024, and the ionic radius ratio between lithium ions and oxygen ions $r(Li^{+})/R(O^{2-})$ is 0.7143, the two octahedral sites in $LiMeO_2$ are filled with transition metal ions and lithium ions.

A transition metal has five d orbitals: z^2, x^2-y^2, xy, xz, and yz. d orbitals are divided into e_g groups for z^2, x^2-y^2, and t_{2g} groups for xy, xz, and xy according to their symmetry. When a transition metal is placed in the octahedral site, the e_g group on the axis becomes unstable, and the t_{2g} group on the plane becomes relatively stable. As a result, d orbital has the electron configuration shown in **Figure 3**. The oxidation state of the transition metal ion is 3+ in $LiMeO_2$. In the case of Co^{3+}, 6 electrons are filled in all three t_{2g} orbitals, making lithium cobalt oxide ($LiCoO_2$) the most stable. The LiO_2 layer and the CoO_2 layer alternately exist in the structure of $LiCoO_2$ shown in **Figure 4**. Although $LiCoO_2$ has a theoretical specific capacity of 274 mAh g^{-1}, the practical capacity is low than the theoretical value. Since when it is charged over 4.2 V vs. Li/Li^+, i.e, when more than half of the lithium ions in the structure are extracted, an irreversible phase transition from hexagonal to monoclinic occurs due to the increase in repulsive force between oxygen layers. Since lithium ions cannot be inserted/desorbed reversibly, the actual usable capacity is limited to 140 mAh g^{-1}, which is half of the theoretical capacity.[14-16]

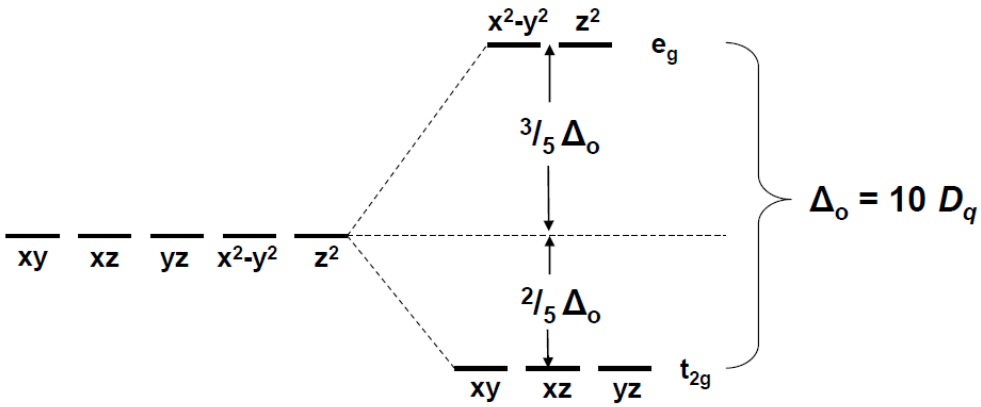

Figure 3. The e_g and t_{2g} d orbital configurations in the octahedra coordination.

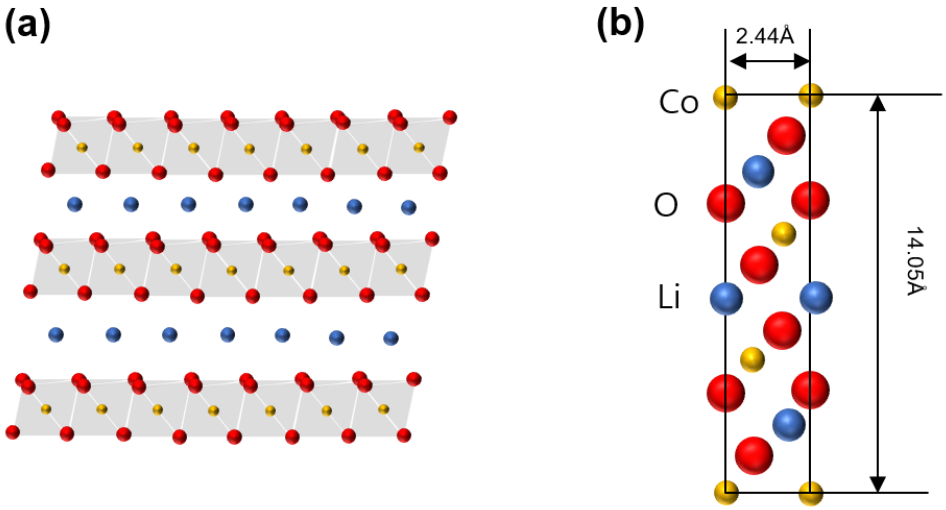

Figure 4. (a) The layered structure and (b) the unit cell of $LiCoO_2$.

2.3.2. Ni-rich layered oxide

To increase the energy density of lithium secondary batteries, it is necessary to develop a cathode material with a practically usable capacity of over 140 mAh g^{-1}. It is reported that the practical capacity increases when cobalt ions are replaced with nickel ions in layered oxide.[18] Especially, a cathode material with more than 80% Ni ion, called a Ni-rich layered oxide, has a practical capacity of 200 mAh g^{-1}.[23-26] Meanwhile, the price of cathode materials is the most dominant for the price of a secondary battery. The recent rapid price increase of cobalt precursor caused a rising price of secondary batteries. In this situation, the price of the secondary battery can be lowered by using an inexpensive Ni-rich cathode material. Although Ni-rich layered oxide has many advantages, there are hurdles to overcome.

First, Ni-rich layered oxide has a lot of residual Li impurities on the surface. Because of the similar ionic radii between Li ions (76 pm) and Ni^{2+} ions (69 pm) and relatively stable Ni^{2+} ions, Ni ions migrate to the Li layer of the structure to form a non-stoichiometric phase.[39-41] Ni ions in the lithium-ion layer hinder the diffusion of lithium ions. Excess lithium is needed for the mitigation of this phenomenon. As a result, the unreacted Li precursor remains on the surface as LiOH

and Li_2CO_3.[18] The Li impurities are electrochemically decomposed during charging, generating gas molecules.[45, 46] This phenomenon causes battery swelling. Also, LiOH is reacted with $LiPF_6$ salt, forming fluoric acid.[47, 48] The acid attacks cathode and anode materials, degrading the cells. On the other hand, LiOH and Li_2CO_3 induce the dehydrofluorination of polyvinylidene fluoride (PVdF), which occurs when the polymer meets the base, causing gelation of the slurry.[49] The most effective method for removing residual impurities is washing with water. However, washing cause degradation of Ni-rich layered oxide.[50-52]

Second, high-volume change causes microcracks for Ni-rich layered oxide. Unlike $LiCoO_2$, which is directly synthesized from the solid-sate reaction using Lithium and cobalt precursor, a NCM precursor is prepared using co-precipitation for uniform transition metal distribution and is thermally lithiated for the final product. As a result, a NCM cathode material has a secondary particle that consists of aggregated primary particles.[53, 54] Although the a-axis lattice change during charging is almost equal, the c-axis lattice severely shrinks with increasing Ni ion contents.[55] This anisotropic volume change causes microcrack generation along with grain boundary. Once cracks are formed, electron transport is hindered. Also, the electrolyte can penetrate secondary particles and is

decomposed on the new surface.[56, 57] Therefore, side reactions on the grain boundary trigger crack propagation.

2.4. Self-assembled monolayer

Self-assembled monolayers (SAMs) are a unique technique to deliver thin layers on a solid surface. SAMs consist of functional, linker, and spacer groups in **Figure 5**. The properties of substrates such as contact angle or work function are controlled by changing the proper functional group.[63, 64] The layers derived from SAMs are formed by spontaneous reactions between the head group and substrates, and they are divided into three reactions depending on the type of the linker (reacting) group of the SAMs. The carboxylate and phosphate groups form an ionic bond with the substrate, the thiol group forms a bond with the substrate by a charge transfer mechanism, and the silane group covalently bonds with the substrate. In general, SAMs having silane groups are used in the case of oxide substate.[65] The dehydration reaction occurs during the process. The space group connects the two groups and controls the layer length and packing density.

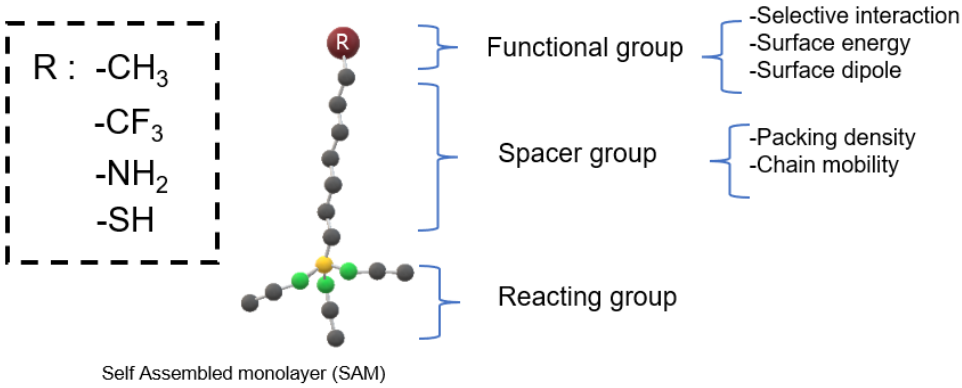

Figure 5. The molecular structure of self-assembled monolayer.

3. Experimental section

3.1. Interfacial modification of Ni-rich layered oxide

3.1.1. Interfacial modification using aqueous solution

The cathode materials of $LiNi_{0.88}Co_{0.06}Mn_{0.06}O_2$ (NCM88) was provide from the Research Institute of Industrial Science & Technology.

For surface modification, 0.1 g of $Mn(SO_4)\cdot H_2O$ was dissolved in 10 ml of deionized (DI) water for 10 min at 5°C. 10 g of NCM88 was poured in this solution and stirred for 5 min. To obtain the surface modified NCM88 powders, the solution was filtered to remove aqueous solution and the remain powder was dried under vacuum oven for 2 hrs at 80°C. The dried NCM88 powders were calcinated at 600°C and 800°C for 3hrs (denoted as LMO-600 and LMO-800)

For comparison with and without manganese precursor, NCM88 powers were washed using DI water, to confirm surface and structural change depending on washing time 10 g of NCM88 was stirred with 10 mL of deionized water for various time of 5, 10 min, 12 hrs, 24 hrs or 48 hrs. To check the influence of H^+ concentration, the powder washed with ethanol for 48 hrs. The washed NCM88s

was filtered and dried under vacuum under same condition with the surface modification method. The filtered powders after 5 min wash powders were subsequently calcinated at 600°C and 800°C for 3 h under an O_2 atmosphere (Wash−600 and Wash−800, respectively).

3.1.2. Interfacial modification using self−assembled monolayer

Ni−rich layered oxide cathodes, $LiNi_{0.82}Co_{0.09}Mn_{0.09}O_2$ (NCM82) was synthesized by a co precipitation assisted solid state reaction. First, transition metal precursors, $Ni_{0.82}Co_{0.09}Mn_{0.09}(OH)_2$ was prepared using coprecipitation method $NiSO_4 \cdot 6H_2O$, $CoSO_4 \cdot 7H_2O$, and $MnSO_4 \cdot H_2O$ are used for Ni, Co and Mn sources, respectively. Second, the precursors were blended with $LiOH \cdot H_2O$ at a 1:1.05 molar ratio using a mortar pestle and the mixed powders was calcined at 750°C in an O_2 atmosphere.

Prior to treating the NCM82 surface, the NCM82 particle was exposed to UV/O_3. A vapor deposition method using octyltrichlorosilane (OTS, Tokyo Chemical Industry Co.) was applied to modify the surface of NCM82 powders. 5 g of NCM82 powders and an aluminum reservoir containing 1 ml of OTS were loaded into a glass petri dish. The glass petri dish was moved inside a vacuum chamber and left overnight. For a spontaneous assembly of OTS, the

temperature in the chamber was kept at 30°C. Inert gas condition with nitrogen was applied to remove unreacted OTS vapor. Next, the NCM82 particle was annealed at 130°C for 1hr. The OTS treated NCM82 denoted as OTS-NCM82.

3.2. Electrochemical analysis

3.2.1. Electrode fabrication

To prepare the composite electrode, the cathode materials were homogeneously mixed with a conducting agent of Denka Black for electron transport channel and a binder of polyvinyl difluoride (PVdF, KF1100, Kureha) at a weight ratio of 96:2:2. The viscosity of the slurry was controlled by adding N-methylpyrrolidinone solvent (Aldrich) to the slurry mixture. The mixture was mechanically mixed using PDM-300 automatic mixing equipment (KM tech) at 1000 rpm 4 times for 210 s. The slurry was cast on Al foil of current collector using bar coater and dried in a convection oven for 10 min at 120°C. The electrodes were press using a roll-press machine (Rohtec) to obtain a density of 3.0 ~ 3.3 g cm^{-3}.

3.2.2. Galvanostatic charging and discharging

All electrochemical performances were evaluated by fabricating 2032 coin type half cells made up with the prepared composite cathodes and lithium foil. To block direct contact between the two electrodes, a polypropylene separator was inserted between cathode and anode. 1 M of $LiPF_6$ in a mixture of diethyl carbonate and ethylene carbonate (1:1 ratio by volume) was used as the electrolyte (Panaxetec, South Korea). All 2032 coin cells were assembled in an argon filled glove box. All cycling performances were evaluated using a battery cycler (LAND CT2001A, China). All rate capability tests and galvanostatic intermittent titration technique (GITT) were conducted using WBSC-3000 (WonATech, Korea). All electrochemical tests were conducted at 25°C.

The half-cells with NCM88s cathodes were charged to 4.25 V vs. Li/Li^+ at 0.2 C (1C = 200 mA g^{-1}) and a constant potential of 4.25 V was applied until the current density decayed to 0.005 C (CC-CV mode) and discharged to 2.5 V vs. Li/Li^+ at 0.2 C for first cycle. The cells were charged and discharged at the same voltage condition with a different current density of 0.3 C vs. Li/Li^+ from second cycle. To confirm Ni doping in Li_2MnO_3 layer, the cells were charged to 4.9 V vs. Li/Li^+ at 0.025 C. For the rate performance test, the cells were

charge to same condition to first charging and discharged at 0.2, 0.5, 2.0, 5.0 and 10 C.

For cycleability test, the half-cells with NCM82s cathodes were charged to 4.3 V vs. Li/Li^+ at 0.2 C (1C = 200 mA g^{-1}) and discharged. From the second cycle, the cells were charged and discharged at 0.3C. The voltage range is the same as that of the first cycle. For GITT curves, after charging a current density of 0.2 C for 30 mins, the rest step was followed for 60 mins to observe the stabilizing potential curves. This charge and rest sequences were repeated for 12 times.

The half-cells with NCM90s were charged in the CC/CV mode. First, the cells were charged to 4.3 V vs. Li/Li^+ in the galvanostatic mode under a constant voltage of 0.2 C, and a constant voltage of 4.3 V was applied until the current density became less than 0.05C (1C = 200 mA g^{-1}). Subsequently, the cells were discharged to 2.5 V under 0.2 C. After the initial cycle, the cells were charged and discharged under 0.5 C, and the CV condition and voltage range were the same as in the first cycle. For rate capability test, the cells charged same condition and discharged under 0.2, 0.5, 1.0, 2.0, 10 and 20 C.

3.2.3. AC electrochemical impedance spectroscopy

Electrochemical impedance spectroscopy (EIS) measurements were

performed using a Ziva Lab MP2 (Won-A-Tech, South Korea) with a voltage amplitude of 5 mV in the frequency range of 100 kHz to 0.01 Hz.

3.3. Materials Characterization

The crystal structures of the cathode materials before and after the surface modification treatment were confirmed by X-ray diffraction using a Rigaku SmartLab diffractometer with Cu Kα radiation in a 2θ range of 10~80° at a scan rate of 5° min^{-1}. The surface morphologies of the prepared powders were observed via field emission scanning electron microscopy (FE-SEM, JEOL, JSM 7800F, Japan). Additionally, transmission electron microscopy (TEM, FEI, TALOS F200X, UK). XPS (PHI 5000 VersaProbe II, UK) was performed with an X-ray Al anode as the source to analyze the chemical state of the electrode surface. The binding energies were calibrated to the C-C peak in C 1s at 285 eV. The surface is etched using Ar ion beam for depth profiling. The chemical compositions of cathode materials were investigated by ICP-OES (Optima 7300DV, PerkinElmer). The lithium impurity content in the prepared samples was analyzed using an auto-titration instrument (848 Titrino Plus, Metrohm). The water and electrolyte contact angles were measured by dropping water and

electrolyte on the pellets consisting of only cathode powders using an S.E.O co. Ltd, Phoenix-MT contact angle meter.

4. Results and discussion

4.1. Interfacial modification with Ni doped Li_2MnO_3

4.1.1. The effect of washing and subsequent calcination

Although it is well known that aqueous washing can significantly reduce the surface lithium impurities in Ni-rich oxides, it degrades the cycliability.[50, 51] **Figure 6a** exhibits the cycle performances of the half-cells with NCM88 cathodes without washing (bare), and that of two washed NCM88s with different washing time (5 min- Wash-600 and 10 min-Wash-600). The three cells had similar specific discharge capacities of 201.0, 203.6, and 201.6 mAh g^{-1} at first cycle (**Figure 6b**). However, the cycling retention of the cells with washed cathodes did not reach that of Bare during the 60th cycles. After 60th cycle, the 5 min-Wash-600 and 10 min-Wash-600 had a discharge capacity of 167.0 and 159.7 mAh g^{-1}, respectively, which were significantly lower than the 192.1 mAh g^{-1} of Bare. Because the lithium ions in the crystalline structure have a high ion affinity, Li^+/H^+ ion exchange takes place during the aqueous washing process. The XRD patterns of the Bare and NCM88s washed under various

circumstances were obtained to figure out the effect of washing with DI water on crystallinity as shown in **Figure 7**. The c-axis of the layered structure was decreased by small H^+ ion insertion throughout the prolonged washing process, as evidenced by the (003) peak shifting to a higher angle with increasing washing time with D.I water. In addition, when compared to the 12-hour wash with water (18.724°), the peak (003) of the 48-hour wash with ethanol (18.706°) was to the left. This is because the concentration of H^+ of water is high compared with ethanol due to the low pKa of H_2O than that of ethanol. In this regard, it was reported that Li^+/ H^+ cation exchange occurred during washing using aqueous solution in Ni-rich cathodes.[50] Thus, the propagation of the H^+-exchanged NiOOH structure from the surface of cathode materials, which was in contact with DI water, is natural. NiOOH was converted into a more stable NiO like phase, which is electrochemically inactive, during subsequent drying and high-temperature annealing processes. More NiO like phase was produced as the washing time gets longer. After washing and drying, we think that vacant Li sites and Ni^{3+} reduction to Ni^{2+} provokes NiO phase production during cycling. As a result, for the 60th cycle, the 10-min-Wash cell showed the lowest level of cyclability among the three samples. However, after the 60th cycle, the capacity of the Bare cell dramatically dropped. The discharge

specific capacity of Bare for the 100th cycle was 109.5 mAh g^{-1}, which was much lower than that of 5-min-Wash and 10-min-Wash (136.5 and 127.2 mAh g^{-1}, respectively). A significant amount of HF was produced as a result of the reaction between the electrolyte and lithium impurity of Bare. It increased the cell's resistance by attacking the SEIs of both the cathode and the anode.[18, 47] Therefore, despite the initial poor cycle ability, the washing procedure is essential for long-term cycling.

Following heat treatments at 600°C and 800°C helped to offset the drawback of washing. The cycabilities and the 1st voltage curves of the half-cells with 5-min-Washs (Wash-600, and Wash-800) are shown in **Figure 8a**. In comparison to Wash-600 (82.0%), the capacity retentions of the Wash-800 cell during the 60th cycle are slightly better at 84.3%. The cycle life was improved by the subsequent high-temperature calcination, but it still not comparable to before washing. (**Figure 8b**) **Figure 9** exhibits the Ni 2p spectra of the Bare, 5-min-Wash, Wash-600, and Wash-800 samples. The Ni 2p peaks can be convoluted according to oxidation state i.e., those of Ni^{2+} and Ni^{3+} at 855.8 and 856.7 eV, respectively.[68] The low Ni^{2+} fraction on the bare surface was 2.2% before washing, however, after washing and 80°C drying, the Ni^{2+} proportion in the 5-min-Wash rose to 30.6%. This is well matched with the findings of an earlier

study on NiO like phase formation. The Ni^{2+} proportions for the Wash-600 and Wash-800 samples reduced to 26.1 at.% and 15.1 at.%, respectively, as indicated in **Table 1**. NiO like phase can reacts with residual LiOH and Li_2CO_3 and forms a Ni-rich cathode material after high-temperature calcination above 600°C, which is the heating condition for synthesizing Ni-rich layered oxide. However, the surface state was not perfectly recovered to the as-synthesized state, because of the deficient Li precursor. The NiO like phase stayed without any reactions. The high Ni intensities of the Ni 2p spectra from all washed samples in contrast to Bare demonstrate that a significant quantity of surface lithium impurities was eliminated. The photoelectron of the Ni component in the active material powder was hindered by a large amount of lithium impurities on the surface, as seen in **Figure 9**. The surface of Ni-rich oxide was exposed after the impurities were eliminated.

Low-magnification FE-SEM images of the cathode materials were obtained to evaluate the particle morphologies of Bare and Wash-800 as shown in **Figure 10a and b**. The washing processes did not dramatically affect the particle shape. All morphologies of secondary particle were preserved with diameters of 10 um. Otherwise, 10 nm of small surface impurity particles were observed in enlarged images of Bare, as indicated by the yellow circles in **Figure 10c**. Fewer

impurities were observed for Wash−800 sample and it exhibited a flat and clean surface. (**Figure 10d**) This agrees with the Ni 2p spectra in **Figure 9**.

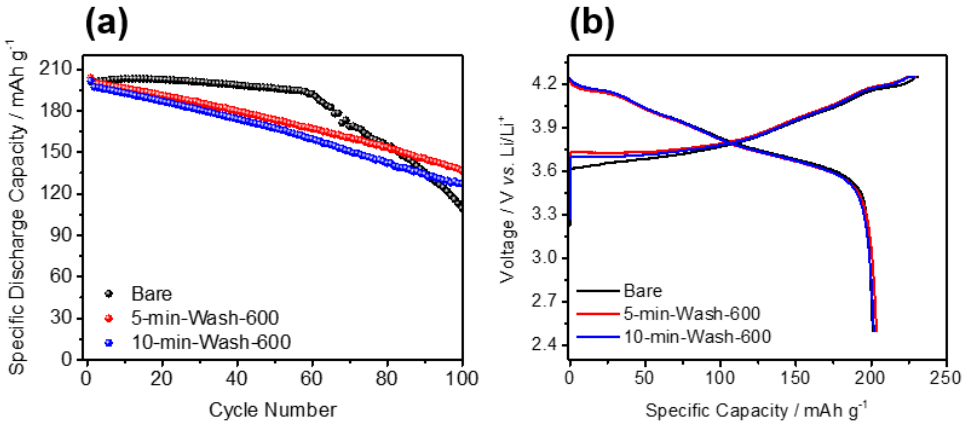

Figure 6. (a) Cycle performances of half-cells of Bare, 5-min-Wash-600, and 10-min-Wash-600.

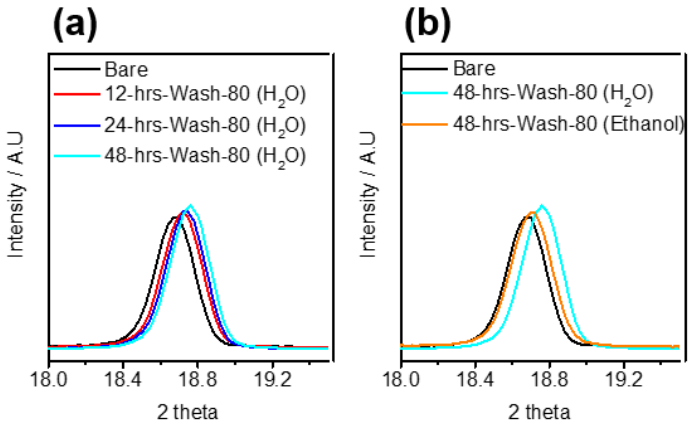

Figure 7. Variations in (003) peak position of XRD patterns depending on (a) the washing time and (b) the different solvent.

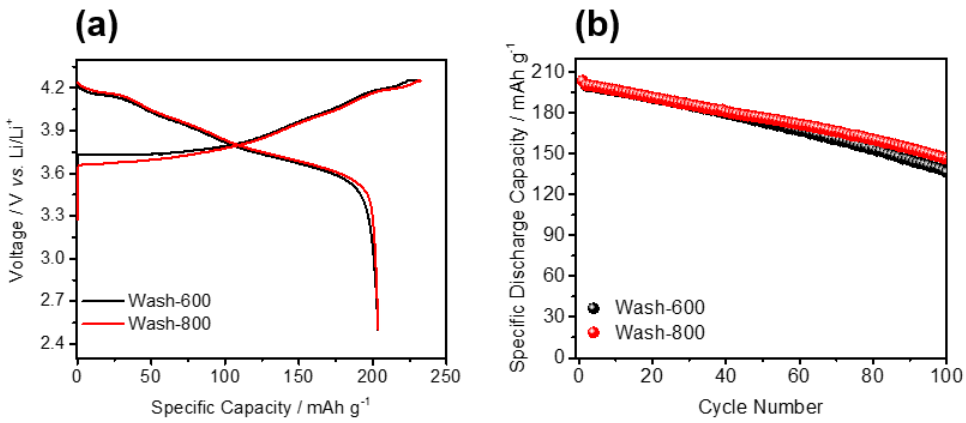

Figure 8. (a) The 1st voltage profiles and (b) cycle performances of Wash-600 and Wash-800 half-cells.

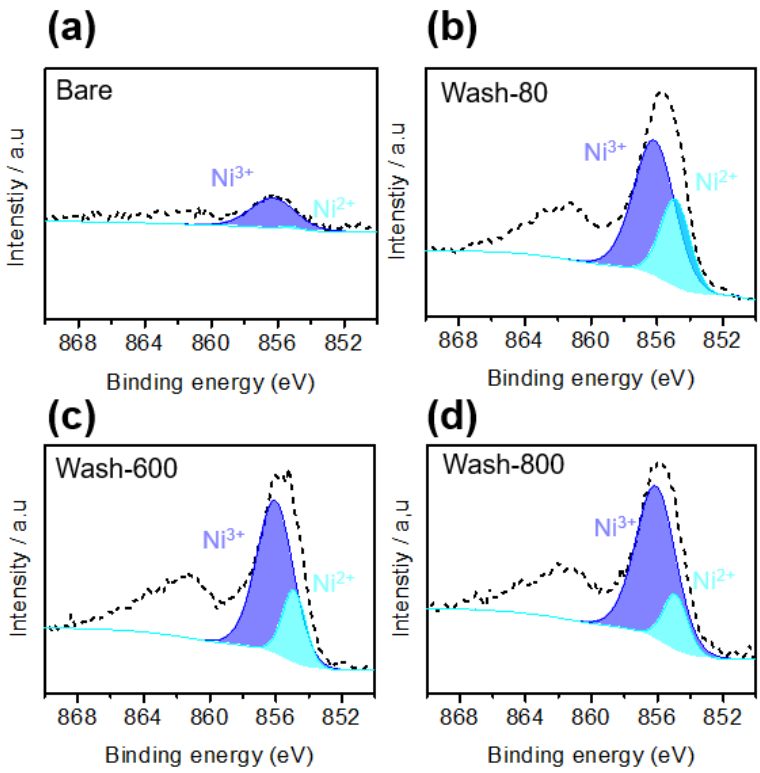

Figure 9. Ni 2p XPS spectra of Bare (a), Wash-80 (b), Wash-600 (c) and Wash-800 (d) powders.

Table 1. Ni^{2+} fraction of Bare, Wash-80, Wash-600 and Wash-800.

	Ni^{2+} fraction
Bare	2.2 %
Wash-80	30.6 %
Wash-600	26.1 %
Wash-800	15.1 %

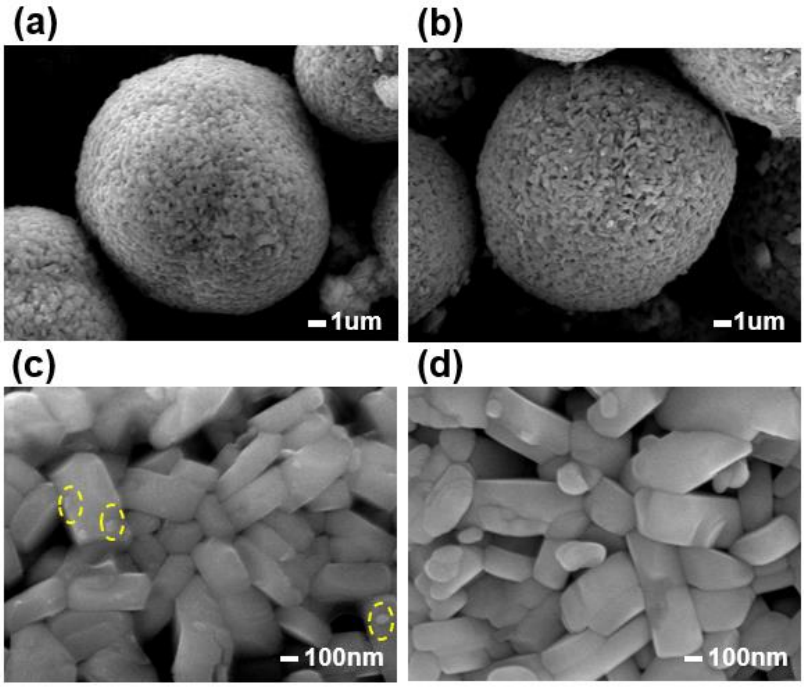

Figure 10. Low and High magnification SEM images of (a and c) Bare, (b and d) Wash-800.

4.1.2. Interfacial modification with Li_2MnO_3

Figure 11a and b show particle shape and size of interfacial modified samples of LMO-600 and LMO-800. The modification procedure also did not change the overall shape and size of cathode materials. Meanwhile, the dramatically different surface morphologies of LMO-600 and LMO-800 were observed i.e., Additional surface passivation was observed. (**Figure 11c and d**) These altered surface morphologies proved that the suggested method, which included stirring in a $MnSO_4$ aqueous solution and annealing, worked well for applying the surface passivation. By increasing the pH from surface basic impurities, the Mn ion in the aqueous solution was precipitated. A uniform surface modification was achieved without requiring specialized tools or treatment.

Meanwhile, distinct crystalline structure of additional surface layer was clearly demonstrated by comparing the surface TEM images of Bare, LMO-600 and LMO-800 cathode powders. (**Figure 12**) A singe d-spacing of 0.473 nm, which relates to the (003) plane of the layered structure was observed for Bare sample. However, LMO-600 and LMO-800 had a new phase with a d-spacing of 0.412 nm, which relates to (110) plane of the Li_2MnO_3 derivative. The inset images of **Figure 12b and c** show the selected area electron

diffraction (SAED) pattern of the outer regions of LMO-600 and LMO-800. Not only an electron diffraction pattern (orange circle) perpendicular to the [100] direction of the layered structure but an additional diffraction pattern (red circle) perpendicular to the [010] or [101] direction of the Li_2MnO_3 phase were observed. It is inferred that the (010) or (101) plane of Li_2MnO_3 phase vertically grew in direction of [100] of layered structure of Bare. Although the doping of Ni ion can change the lattice parameter of Li_2MnO_3, it is difficult to confirm the difference by TEM images. Meanwhile, it was found that the Mn precursor which was precipitated on the surface reacted with lithium impurities to generate a Li_2MnO_3 phase. Finally, it was observed that the surface of Ni-rich layered oxide was covered with Li_2MnO_3 derivates.

In order to confirm that Li_2MnO_3 is formed from the precipitated manganese precursor, Mn_3O_4 was reacted with lithium precursors at 600°C or 800°C. The XRD patterns of the final products were assigned to Li_2MnO_3 (**Figure 13a**). Therefore, the results support that LMO-600 and LMO-800 had Li_2MnO_3 layer on the surfaces. **Figure 13b** shows the XRD patterns of the Bare, washed, and coated materials. The crystal structure of Bare indexed to the R-3m group of a layered structure without any impurity phase. All cathode materials show identical structures. These identical XRD patterns

without bi-phases show that NiO like phase and the coating layer were negligible for detecting by XRD.

The proposed surface modification method is more effective in removing lithium impurities than a simple washing process because the additional layer consumes impurities, forming a lithium-containing layer. **Figure 14** displays the quantity of lithium impurities calculated from the titration method from the impurity dissolved DI water stirred with Bare, Wash-800, and LMO-800 powders. 12204 ppm of LiOH and 5400 ppm of Li_2CO_3 were present in Bare and Washing successfully decreased these quantities to 4423 ppm and 2140 ppm, respectively. These impurities were further reduced to 3103 and 1072 ppm, respectively, by the surface modification process, which was more effective than the simple washing.

To carefully investigate the surface of cathode materials, XPS analyses were carried out. **Figure 15** displays the C 1s, O 1s, Ni 2p and Mn 2p XPS spectrum of Bare, Wash-800, LMO-600, and LMO-800 powders. The C 1s spectra was divided into four peaks: the C-C peak at 285.0 eV, C-O peak at 287.6 eV, C=O peak at 288.1 eV, and CO_3 at 290.2 eV. The lithium impurities of Li_2CO_3 on the surface were main origin of the carbonate peak. The CO_3 peak of LMO-600 and LMO-800 had substantially lower intensities compared to Bare and Wash-800. It demonstrates that Li_2CO_3 impurities decreases by

consuming throughout the reaction between the precipitated Mn precursor and the residual lithium precursors. It was found that the surface modification procedure removed more lithium impurities as compared to washing from the intensity of the carbonated peaks. The Li_2O signal at 528.3 eV was also the most prominent from Bare in the O1s spectra, indicating a considerable quantity of impurity Li_2O. After washing and surface modification using aqueous solution, this peak intensity dramatically dropped. On the other hand, the intensity of the peak corresponded to Me−O bonding at 529.5 eV increased after washing because the surface impurities were removed, exposing the surface of cathode materials. Since the lithium impurities were further decreased to generate Li_2MnO_3 phase, the modified samples, LMO−600 and LMO−800, showed greater Me−O bonding peaks than those of washed material. The washing and coating show a consistent effect for of the Ni 2p spectra. Because plentiful impurities covered the surface, Bare shows an exceptionally low Ni 2p peak. The intensity of the Ni 2p signal of Wash−800, LMO−600, and LMO−800 increased dramatically owing to the removing the lithium impurities. Mn 2p signals were observed only in the Mn 2p spectra of coated samples, LMO−600 and LMO−800, since the Li_2MnO_3 coating was applied on the surface. As the Mn 2p 3/2 peak at 643 eV overlapped with the Ni Auger peak,[69] only peak of Mn 2p 1/2 at 654 eV is

meaningful for Mn^{4+} in the Mn 2p spectra. Mn 2p 1/2 photo electron was observed in only two spectra of coating samples, as predicted. It is noteworthy that LMO−800 had the lower Mn 2p 1/2 peak compared to LMO−600, although the same amount of manganese sulfate was used the coating process. It is hypothesized that NiO like phase and additional Li_2MnO_3 phased were merged, especially for LMO−800, since XPS is a surface sensitive tool.

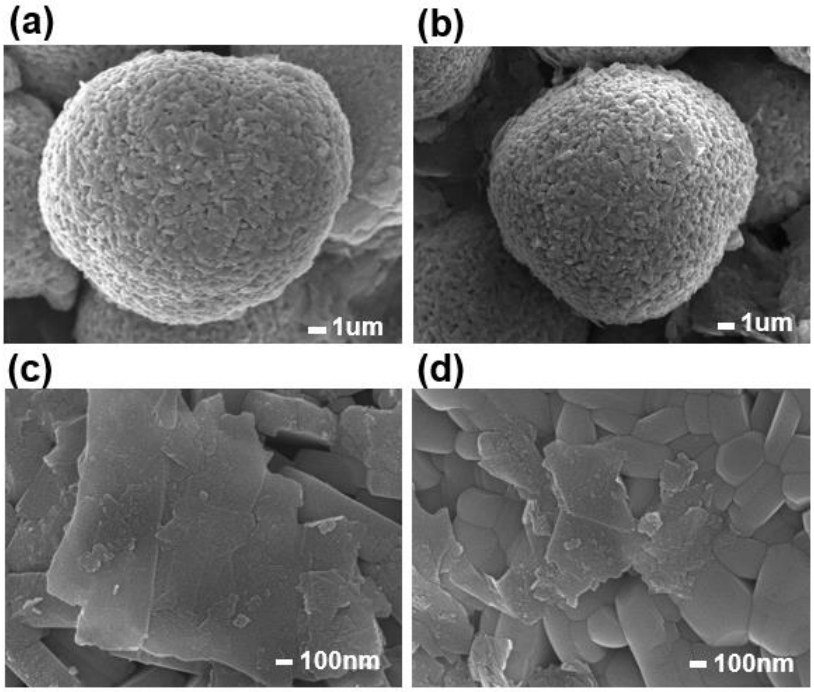

Figure 11. Low and High magnification SEM images of (a and c) LMO-600, (b and d) LMO-800.

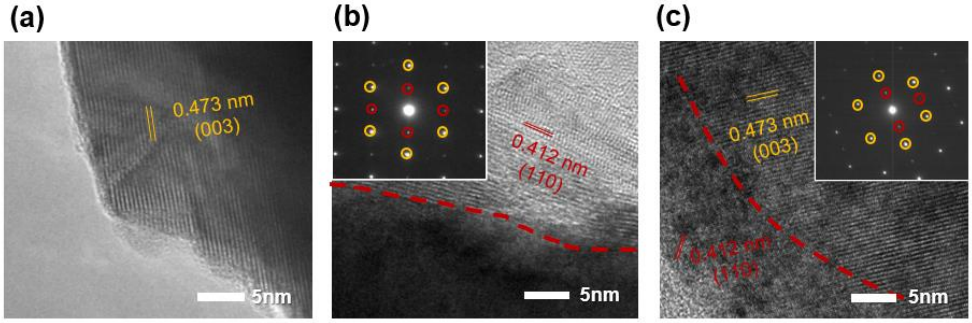

Figure 12. TEM images of (a) Bare, (b) LMO-600 and (c) LMO-800.

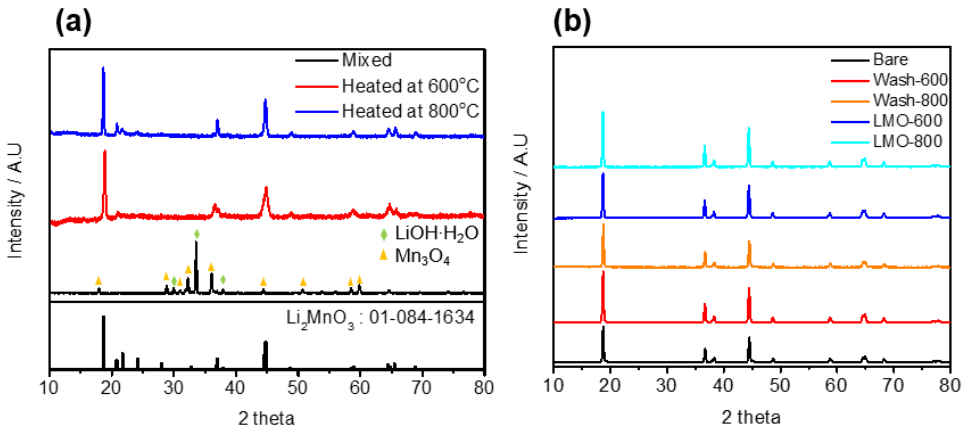

Figure 13. (a) XRD pattern obtained by mixing coating precursors before (Mixed) and after heat treatment at different temperature of 600 and 800°C (b) XRD patterns of Bare, Wash−600, Wash−800, LMO−600, and LMO−800.

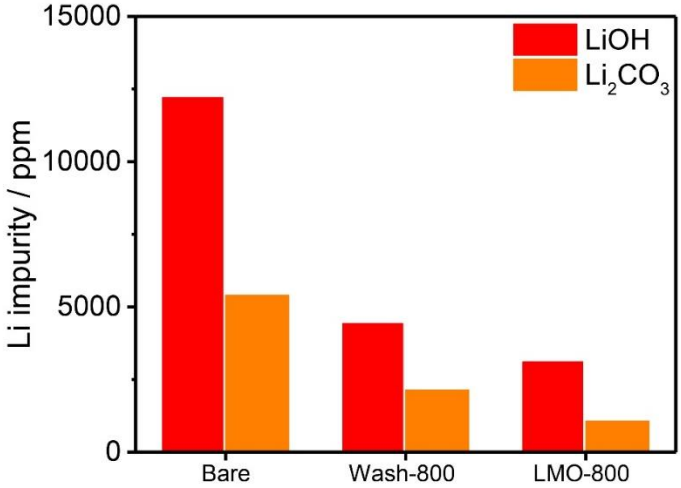

Figure 14. Amounts of LiOH and Li_2CO_3 calculated by the titration of Bare, Wash−800, and LMO−800.

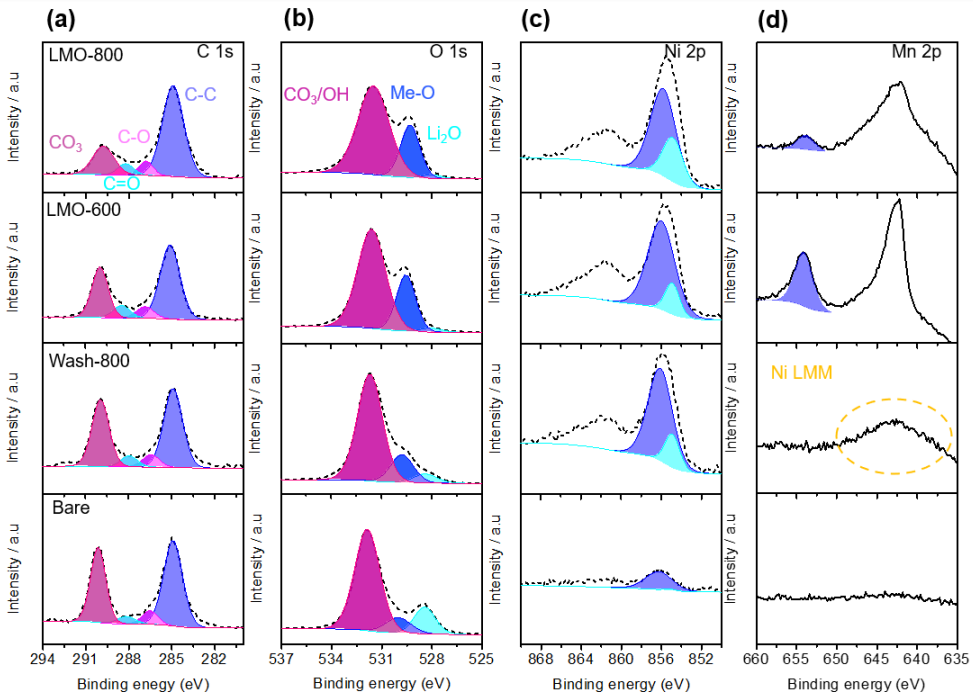

Figure 15. XPS spectra for (a) C 1s, (b) O 1s, (c) Ni 2p, and (d) Mn 2p of Bare, Wash-800, LMO-600, and LMO-800.

4.1.3. Ni doping in Li_2MnO_3

To confirm Ni doping into the Li_2MnO_3 layer, line energy dispersive spectroscopy (EDS) was performed. Line EDS results reveal that LMO-600 and LMO-800 shows the different atomic depth profiles of Ni and Mn. An additional coating layer where only Mn without Ni was founded was observed for LMO-600 as exhibited in **Figure 16a**. The Mn intensity almost disappeared whereas Ni intensity increased near the surface region, revealing that the separation of Li_2MnO_3 from the Ni-rich cathode material. In contrast, **Figure 16b** depicts the combining of Mn and Ni signals at a thickness of 100 nm. This special atomic depth profile indicates that LMO-800 had Ni ions doped Li_2MnO_3 coating layer. The ToF-SIMS results of the surface modified cathode materials, LMO-600 and LMO-800 is displayed in **Figure 17**. In general, the result indicates that the surface sputtered for 300 s had more MnO_2^-intensities. It means that the surface was covered with Mn-abundant Li_2MnO_3 phase. LMO-600 had more distinguishable Ni and Mn intensity profiles than LMO-800. For LMO-600, the normalized intensity of MnO_2^- was recorded as 100% at a sputtering time of 125 s, and the intensity decreased to 34.3% after 1800 s of the sputtering. the normalized Ni-secondary ions increased to 100% at the sputtering time of 1800 s. The increasing

slope of Ni ions was verified based on a 540 s sputtering time for 50% of Ni ions. In the case of LMO−800, the normalized MnO_2^- was retained as a value of 73.5% after 1800 s of the sputtering time after the 100% recording at the sputtering time of 200 s. This indicates Mn was diffused to Ni−rich matrix. Also, the presence of Ni was more pronounced in the Mn−rich region, providing that NiO like phase and Li_2MnO_3 layer are merged to form Ni−doped Li_2MnO_3 structure in LMO−800.

It was reported that Ni^{2+} ions were doped in 2b of Li^+ site for Li_2MnO_3 through structural analyses and STEM images.[70−72] Unlike Li_2MnO_3, which begins redox reaction at 4.4 V vs. Li/Li^+,[73−74] it takes place at 4.6 V for Li_2MnO_3 doped with Ni^{2+} at 2b site.[70, 75, 76] These different reaction potentials allow the electrochemical assignment of Ni^{2+} ion doping. The half−cells with Wash−800, LMO−600, and LMO−800 cathodes were charged to high cut−off condition of 4.9 V vs. Li/Li^+ at 0.025 C to examine the voltage curve of the Ni doped Li_2MnO_3 coating layer. The voltage profiles of cells were shown in **Figure 18a.** Unlike other samples, LMO−800 had a plateau (green circle) around 4.65 V. This is clearly demonstrated by the calculated $dQ\ dV^{-1}$ plots as indicated in **Figure 18b**. Wash−800 and LMO−600 did not show any peaks, while LMO−800 had a novel differential peak at 4.65 V vs. Li/Li^+, implying delithiation process. It was confirmed

that Ni ions were incorporated into Li_2MnO_3 during the high-temperature annealing for LMO-800 through the delithiation potential of Ni-doped Li_2MnO_3 at 4.65 V vs. Li/Li^+.[70] It is consistent the previous result that the peak shifting occurs only under the synthesis condition over 800°C.[77] Ni doping into Li_2MnO_3 is considered very successful in alleviating the failure mechanism of Ni-rich layered oxides in relation to the unfavorable NiO like phase generation induced by the washing process.

Figure 19a presents the cyclablities of the Wash-800, LMO-600, and LMO-800. The half cells with LMO-600 and LMO-800 electrodes had comparable discharge capacities of 198.8 and 191.6 mAh g^{-1} at the first cycle, respectively. Since the oxidation state of Ni ions on the surface is depending on post-calcination temperature, the effect on capacity retention of both coatings can be confirmed by comparing NCM88s treated at the same temperature. LMO-600 showed a capacity of 140.1 mAh g^{-1} after the 100th cycle, making the capacity retention 70.5 %, which is higher than 67.0 % of Wash-600 (**Figure 6**). It indicates that Li_2MnO_3 coating alleviates surface degradation. For LMO-800, a high capacity of 167.0 mAh g^{-1}, establishing capacity retentions of 87.2% after the 100th cycle, which is much higher than that of Wash-800 (72.0 %).

Although both coatings prevent electrolyte decomposition, the

improved performance of the LMO-800 is due to an additional function. NiO like phase remained on the surface for LMO-600. In contrast, the bi-phase formed after stirring with an aqueous solution and heating was removed and combined with the coating layer throughout the high-temperature calcination for LMO-800. As a result, the cycle performance of LMO-800 showed enhanced capacity retention because Ni doping in the Li_2MnO coating layer not only suppresses surface side reaction but also reduces the impurity phase. **Figure 19b** exhibits the rate capability tests evaluated on the Bare, Wash-800, LMO-600, and LMO-800 half-cells at various discharge current densities of 0.2, 0.5, 2.0, 5.0, and 10C. The results reveal that Wash-800 and LMO-600 shows inferior performance compared to Bare. The NiO like phase created during the washing and coating procedures, which hindered lithium ions and electrons transport on the surface, is responsible for this worsen rate capability. This indicates that common washing and coating techniques were insufficient in mitigating the surface degradation modes. However, because the inactive NiO like layer was relieved by the Ni doping in coating layer, the cell with LMO-800 electrode exhibited higher capacity under the high current density of 10 C than Bare.

The dQ dV^{-1} curves obtained from the voltage curves of cell with Wash-800, LMO-600, and LMO-800 are displayed in **Figure 20**.

When charged, the Ni-rich layered oxides experienced a variety of redox processes that were related to phase transformations. Initially, the hexagonal structure changed to a monoclinic structure at 3.6 V vs. Li/Li^+, and further Li extraction resulted in a change from a monoclinic structure to a second hexagonal structure at 4.0 vs. Li/Li^+. Finally, this phase was transformed to a third hexagonal structure at 4.2 V vs. Li/Li^+.[55] As the cycle progressed, all peaks related to phase change of Wash-800 and LMO-600 polarized gradually or disappeared, while the peaks of LMO-800 were maintained during the repeated cycle.

Figure 21 exhibits EIS tests of Bare, Wash-800, LMO-600, and LMO-800 at the 1st and 60th charging. According to the equivalent circuit shown in the inset of **Figure 21a**, two semi-circles were obtained. the diameter of the semicircle on the left side in high-frequency domain reflects the film resistance (R_{film}) and that on the right in the low-frequency region reflects the charge-transfer resistance (R_{ct}). Initially, the R_{film} of Bare, Wash-800, LMO-600, and LMO-800 were comparable as 3.9, 3.6, 3.6, and 3.6 Ω, respectively. However, although surface impurities were removed after washing, due to the surface NiO like impurity phase, Wash-800 and LMO-600 had a larger R_{ct} of 6.8 and 7.1 Ω, respectively, compared to Bare (2.8 Ω). Because NiO like phase was partially eliminated by high

temperature calcination, Wash−800 had a slightly reduced Rct. In the case of LMO−800, the NiO like phase disappeared through Ni doping in the Li_2MnO_3 layer as well as lithium impurities. As a results, LMO−800 had the lowest R_{ct} of 2.3 Ω among all samples. The film and charge transfer resistances rise due to surface side reaction and the generation of NiO phase, which resulted from the reduction of unstable Ni^{4+} and vacant Li^{+} site after charging. The solid electrolyte interfaces (SEIs) was attacked by HF derived from lithium impurities in addition to electrolyte decomposition, raising the film resistance of Bare to 25.3 Ω after the 60th cycling. Meanwhile, all washed and surface modified Ni−rich cathodes showed lower R_{film} than Bare, as well as surface modification mitigated side reaction, alleviating the growth of R_{film} of the coated LMO−600 and LMO−800 after cycling. In the case of charge transfer resistance, NiO phase was easily propagate by NiO like phase which is caused by the reaction between cathode materials and water. Therefore, the R_{ct} of cell with Wash−800 and LMO−600 electrodes were raised to 30.2 and 39.5 Ω, respectively. On the other hand, LMO−800 had the lowest R_{ct} after cycling owing to an inhibition of the increasing NiO phase.

Figure 22 shows a schematic illustration of the surface change of NCM88 in the coating process using a manganese sulfate aqueous solution and subsequent drying and calcination. Li−ion in the

structure was exchanged with the H^+ ion in an aqueous solution during the washing and coating processes, forming a proton-involved NiOOH-like structure. The conventional coating with an aqueous solution is ineffective owing to the impurity phase. Next, the precipitated $Mn(OH)_2$ during the coating process decomposed to Mn_3O_4 and converted to a Li_2MnO_3 coating layer after heating at 600°C through the reaction with the residual lithium impurities. The NiO phase still existed as unreacted at a low temperature of 600°C. However, NiO like phase disappeared by the doping of Ni ions into the Li_2MnO_3 layer at a high temperature of 800°C

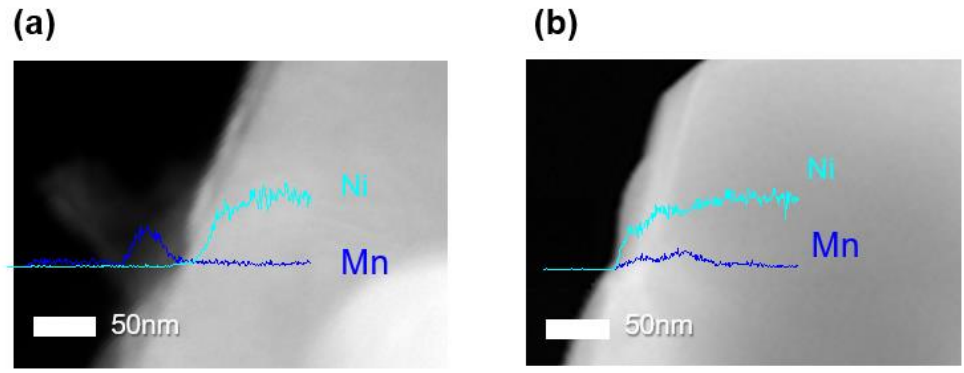

Figure 16. STEM images with line EDS results of Ni and Mn for (a) LMO-600 and (b) LMO-800.

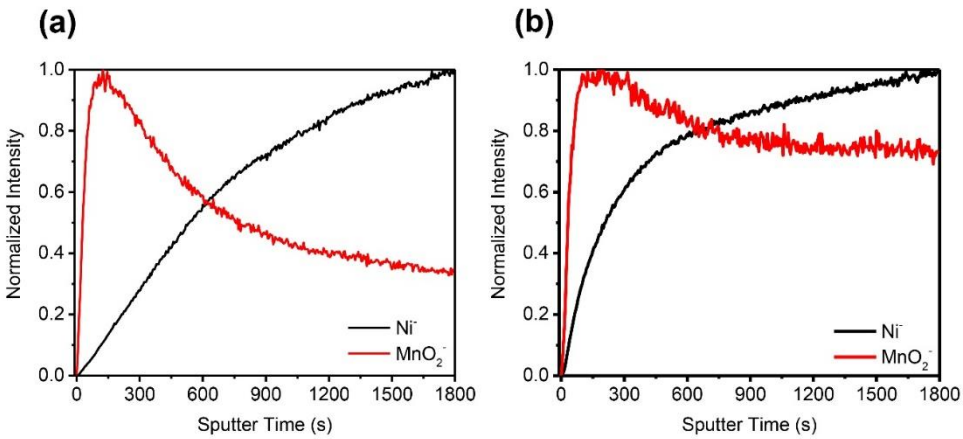

Figure 17. ToF-SIMS depth profiles of Ni^- and MnO_2^- ions for (a) LMO-600 and (b) LMO-800.

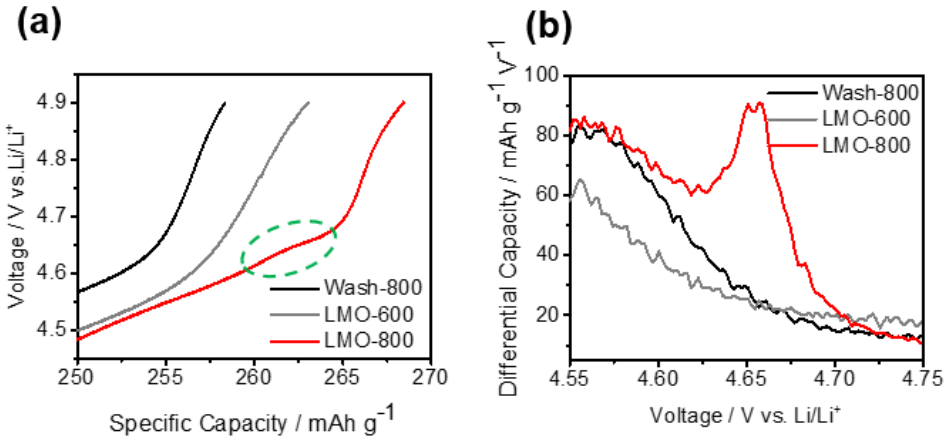

Figure 18. (a) The voltage curves up to 4.9 V vs. Li/Li^+ and (b)Calculated dQ dV^{-1} curves of Wash-800, LMO-600, and LMO-800 half-cells.

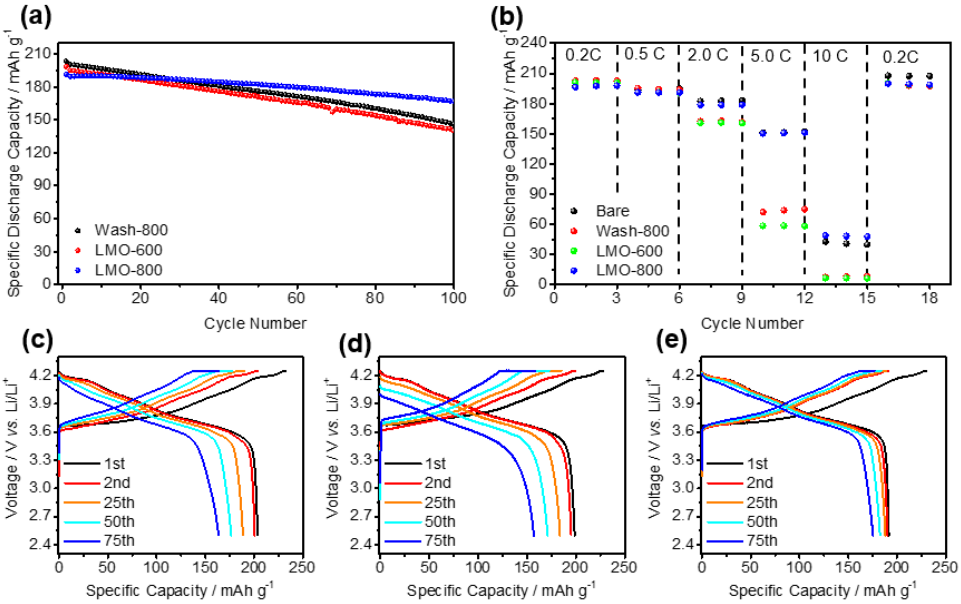

Figure 19. (a) Cycling performances of Wash-800, LMO-600, and LMO-800 half-cells at 25°C. (b) Rate capability tests of Bare, Wash-800, LMO-600, and LMO-800 half-cells. Voltage profiles of half-cells with (c) Wash-800, (d) LMO-600, and (e) LMO-800 cathodes from the 1st to 75th cycles.

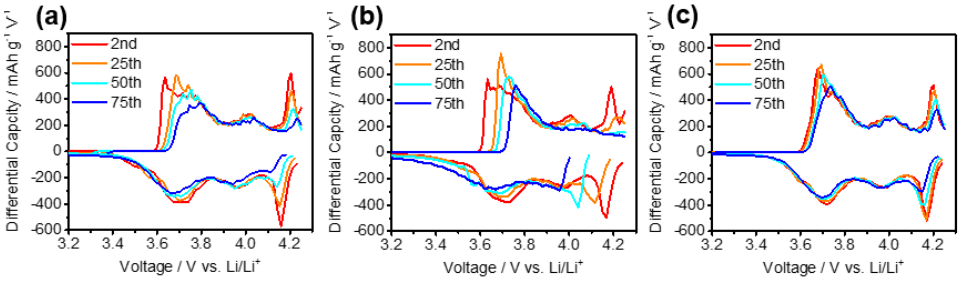

Figure 20. dQ dV^{-1} curves calculated from the voltage profiles of (c) Wash-800, (d) LMO-600, and (h) LMO-800.

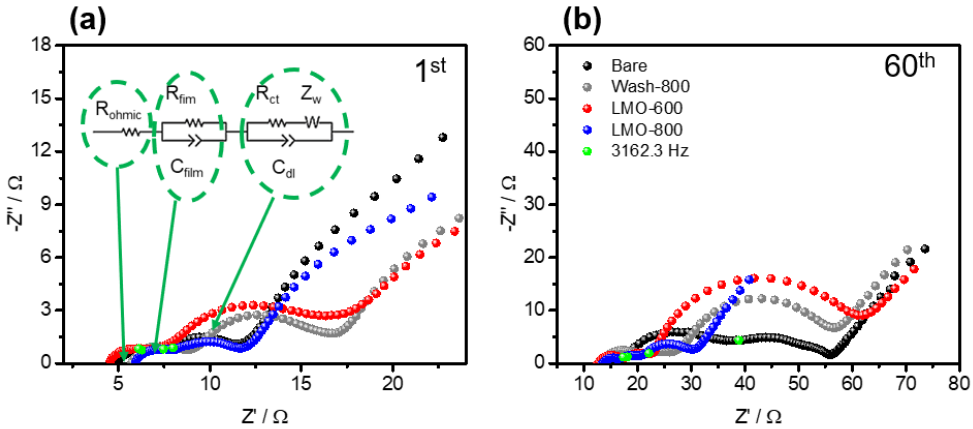

Figure 21. Nyquist plots of fully charged cells at 4.25 V vs. Li/Li^+ for Bare, Wash-800, LMO-600, and LMO-800 half-cells after (a) 1st and (b) 60th cycles. Inset shows equivalent circuit.

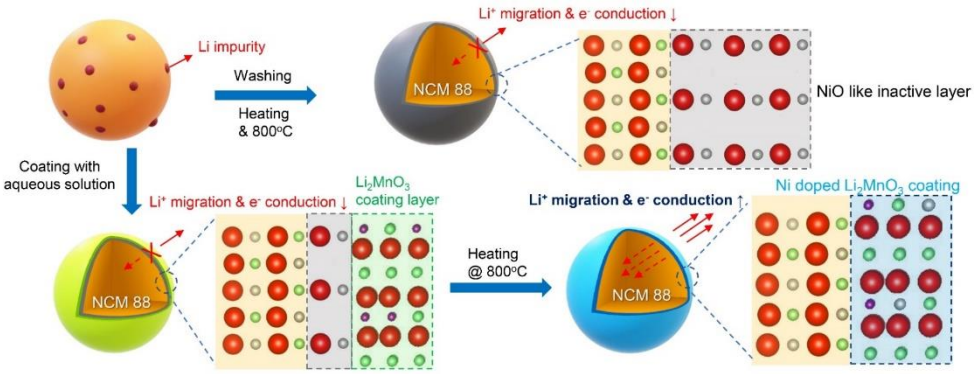

Figure 22. Schematic illustration of Ni-doped Li_2MnO_3 coating process.

4.2. Electrolyte-phobic interfacial modification with aliphatic molecular interfacial modification

4.2.1. Electrolyte-phobic surface monolayer.

The molecular architecture of OTS SAM is shown in **Figure 23a**. The precursor having long aliphatic group was chosen since this long hydrocarbon group exhibits non-polar property which is relatively resistive to the polar electrolyte. A schematic illustration of the molecular surface changes by a simple gas phase reaction of OTS is shown in **Figure 23b**. First, Si-Cl, the reacting group in OTS precursor, is readily changed to Si-OH. Next, it forms a Si-O-Me bond through the hydrolysis reaction between the transformed reacting group and the native hydroxide on the surface of cathode material. The neighboring site on the active material follows the same sequence, resulting in a uniform layer from OTS covering the surface. Only a single layer was established because of its alkyl-terminated end group, which is not reacted with additional precursor, as shown in **Figure 23**. Several grains composed of ordered alkyl chain grains tilted 10-15° toward the surface of the active material are produced by the van der Waals force between adjacent OTS molecules.[62]

Finally, the remaining Si−OH group without any bonding is coupled with the Si−OH group of the adjacent molecule from OTS through the annealing process at a temperature of 130°C, resulting in a uniform surface layer of Si−O−Si−O bonds. Hydrolysis occurred during the thermal annealing process, resulting in the strong Si−O−Si bonding between the close molecules from OTS.[63] Since the high temperature calcination causes cation mixing and NiO phase,[78] the mild temperature of 130°C is suitable for Ni−rich layered oxide.

XRD patterns of cathode materials were displayed in **Figure 24**. The XRD pattern of Bare−NCM82 was confirmed as the R−3m space group. After the surface modification, OTS−NCM82 had the same crystallin structure as Bare. These XRD patterns showed that OTS precursor only reacted with the surface of the cathode material while the original layered structure is maintained.

Figure 25 showed the FE−SEM images of two cathode materials. Since the cathode precursor was usually synthesized by a coprecipitation technique for a uniform transition metal distribution, Bare−NCM82 showed secondary particles with diameters of ~10 um where the primary particles are aggregated (**Figure 25a and b**). OTS−NCM82 had the almost same morphology as Bare, which is compatible with the XRD results (**Figure 24**). The Bare−NCM82 had a flat and clean surface, indicating high crystallinity from the high

magnification image in **Figure 25c**. However, the surface of OTS-NCM82 showed a distinctive morphology (**Figure 25d**). In general, the monolayer from OTS treatment is not visible by SEM because the surface passivation from OTS is just a single layer with a thickness of ~ 1 nanometer. However, since OTS treatment changes the surface into an aliphatic molecule with low electrical conductivity, the secondary electrons for electron microscopy is charged on the insulated surface. Therefore, it believed that OTS-NCM82 showed the blurred SEM image as shown in **Figure 25d**. The TEM images of both cathode powders were also exhibited in **Figure 26**. Bare NCM-82 showed a flat surface, while OTS-NCM82 showed 1.1 nm of a thin layer with a distinctive contrast. It was reported that the thickness of the surface film from OTS was 1.0 nm when OTS SAM precursor deposited a molecular layer on the substrates.[79, 80] A 1.1 nm of surface layer supported that the molecule from OTS reacted with the surface of the active material and the strong Si-O-Si-O bonding between the neighboring molecules. It is difficult to deliver the nanoscale coating through a conventional coating process because these methods are achieved by precipitation methods, which provide thick coating layer ranging in thickness from several um to hundreds of nm. As a result of the excessive amount of inactive coating material on the electrode, the conventional coating method

reduces the energy density of the LIB. On occasion, a thick um-scale surface film can inhibit the transport of lithium-ion on the surface, decreasing the capacity. The coating thickness can be down to nm scale in this unique SAM strategy at the molecular layer. The SAM coating effectively resolves the issue by lowering the coating layer in practical applications.

XPS was conducted to examine the surface chemical components before and after OTS treatment. The C 1s signals of the Bare and OTS NCM82 before and after the heat treatment of 130°C were shown in **Figure 27**. The spectra were deconvoluted into three peaks of C-H/C-C at 285 eV, C-O bonding at 288.5 and C=O at 290 eV. The presence of C=O/C-O peaks was thought to be caused from the unavoidable surface impurities, Li_2CO_3. The intensity of the C-H/C-C peak of OTS-NCM82 with or without the baking process of 130°C was raised. The peak increase indicated a long hydrocarbon chain from the surface film by OTS molecule. In addition, the carbonate peak decreased after OTS treatment owing to the surface passivation. Also, the strong observation of Si 2p peak, which was absent in the case of Bare-NCM82, in the top and middle spectra of **Figure 27** for OTS-treated samples clearly supported that the surface of cathode materials was covered with the film by OTS due to silane group in the reacting group of OTS. In O 1s signals, OTS-coated NCM82

without the annealing showed a strong Si−OH peak at 533 eV. The peak decreased for the final product after the heat treatment. Alkyltrichlorosilanes, which were the most explored SAMs, were generally considered to irreversibly connect to the surface and the adjacent SAM molecules by a Si−O−Si−O bonding. The organic monolayer was created by condensation between the SAM molecule and the hydroxyl group of substrates because of the extensive bonding of the anchoring groups to the surface through strong and localized bonds.[81−85]

ICP−OES was evaluated to confirm Si quantitative analyses in cathode materials (Table 2). The transition metals closely matched the NCM82 stoichiometry. The amount of Si of OTS−NCM82 was unavailable for detection, indicating the surface modification from OTS was negligible. Given that the Si 2p peak of OTS−NCM82 was observed by XPS analyses, Si was localized on the surface. This difference between the XPS and ICP−OES analyses demonstrated that only a thin Si−containing surface monolayer was successfully achieved during OTS−SAM coating without losing energy density from a thick coating layer.

The pellets were prepared using only cathode powders to confirm whether OTS treatment changed the surface properties. The electrolyte wettability was evaluated by measuring the contact angle

of the dropped electrolyte on the pellets. The electrolyte directly penetrates the Bare-NCM82 pellet, and the contact angle was measured to be 3.3°. (**Figure 28a**) On the other hand, OTS treatment significantly increased the contact angle to 31.7° (**Figure 28b**) because the non-polar hydrocarbon group is repulsive to the polar electrolyte. In addition, the different surface properties were confirmed by dispersing the cathode powders in a water solvent. **Figure 28c** shows the photo images of the powders poured into water. Bare-NCM82 powder immediately started to disperse and sank to the bottom after pouring, while OTS powder floated on top of the solvent without dispersion. This behavior of coated powder was maintained after 4 hrs. As the case of the electrolyte contact angle, Bare powder spread in water, but OTS-NCM82 powder aggregated in the solvent. Also, it was separated from water, although the particle has a higher density than the water.

EDS mapping with fluorine was performed to obtain the cross-sectional images after soaking in the electrolyte for 24 hrs for enough electrolyte penetration. The cross-sectional SEM images of Bare and OTS-NCM82 is shown in **Figure 29**. In the case of Bare, the red points correlated to F were observed inside the particle. It is thought that the electrolyte has excellent access to the boundary of the primary particle. As a result, the F from $LiPF_6$ is detected in the

center and at the surface of the secondary powder. On the other hand, weak EDS signals from the F atom were observed in the core side of OTS-NCM82. The hydroxyl group of the surface of NCM was covered with alkyl-terminated OTS, resulting in inaccessibility and low surface energy, which is thought as the reason for mitigating electrolyte penetration inside the secondary particles of OTS-NCM82. This supports that the surface film from OTS has an electrolyte-phobic characteristic.

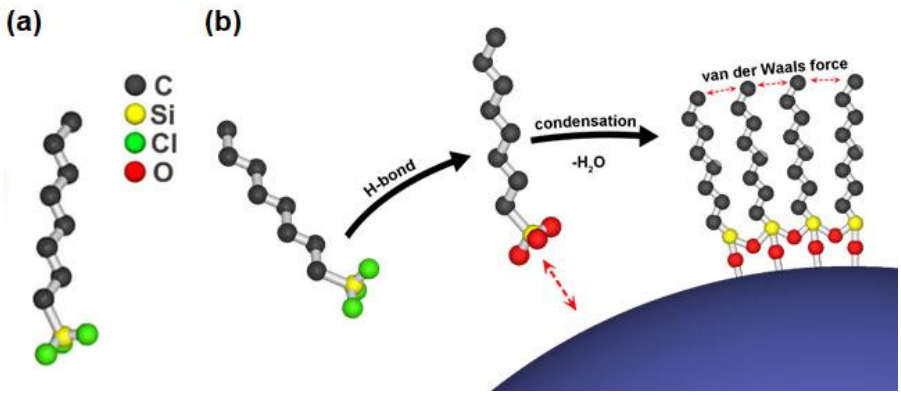

Figure 23. (a) octyltrichlorosilane molecule (b) Schematic illustration representing the self-assembled monolayer coating with octyltrichlorosilane on the Ni-rich oxide cathode powder.

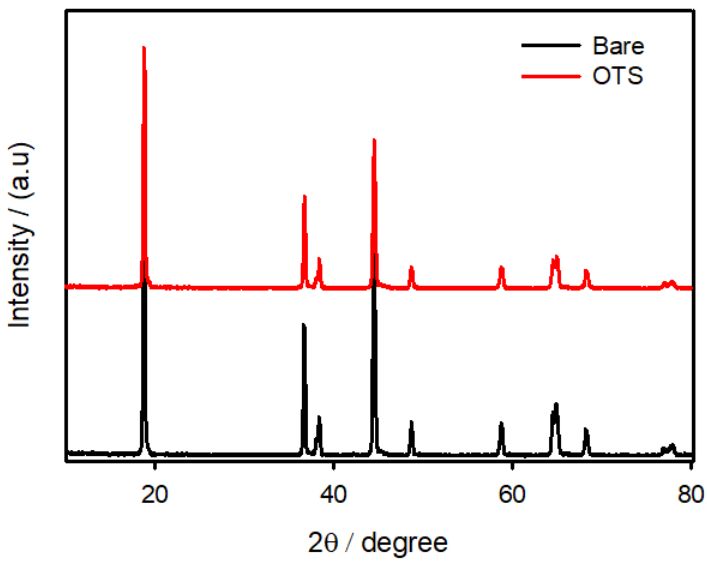

Figure 24. X-ray diffraction patterns of Bare-NCM82 and OTS-treated NCM82.

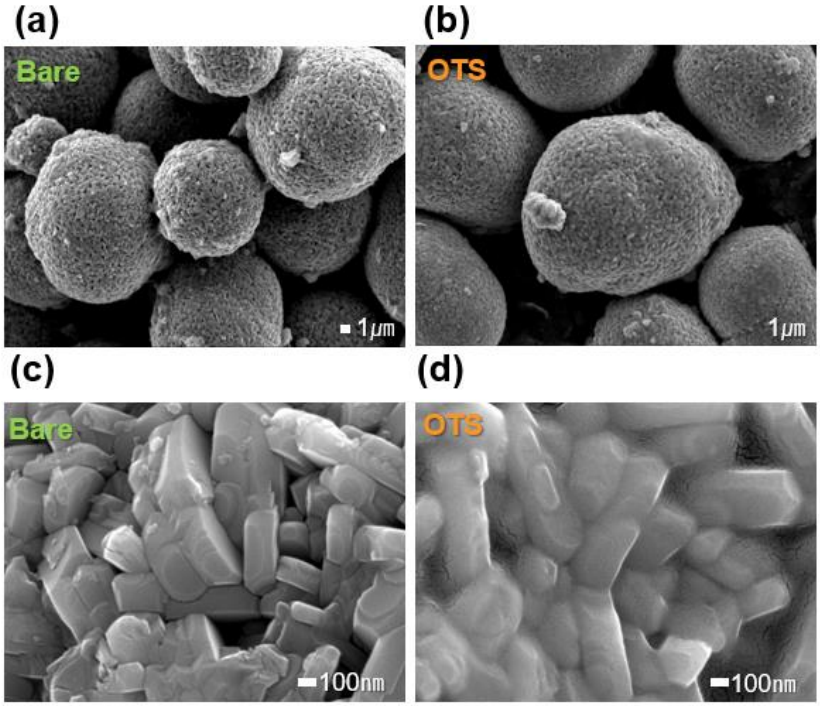

Figure 25. FE-SEM images of (a and c) Bare-NCM82 and (b and d) OTS-NCM82 obtained at low and high magnification.

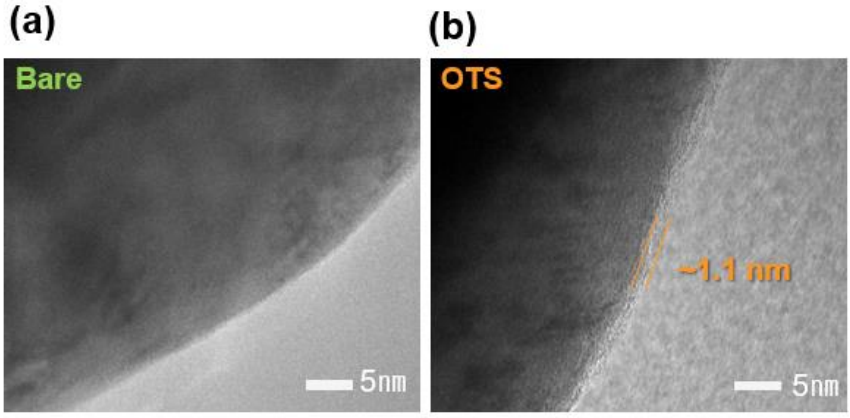

Figure 26. TEM images of (a) Bare-NCM82 and (b) OTS-NCM82.

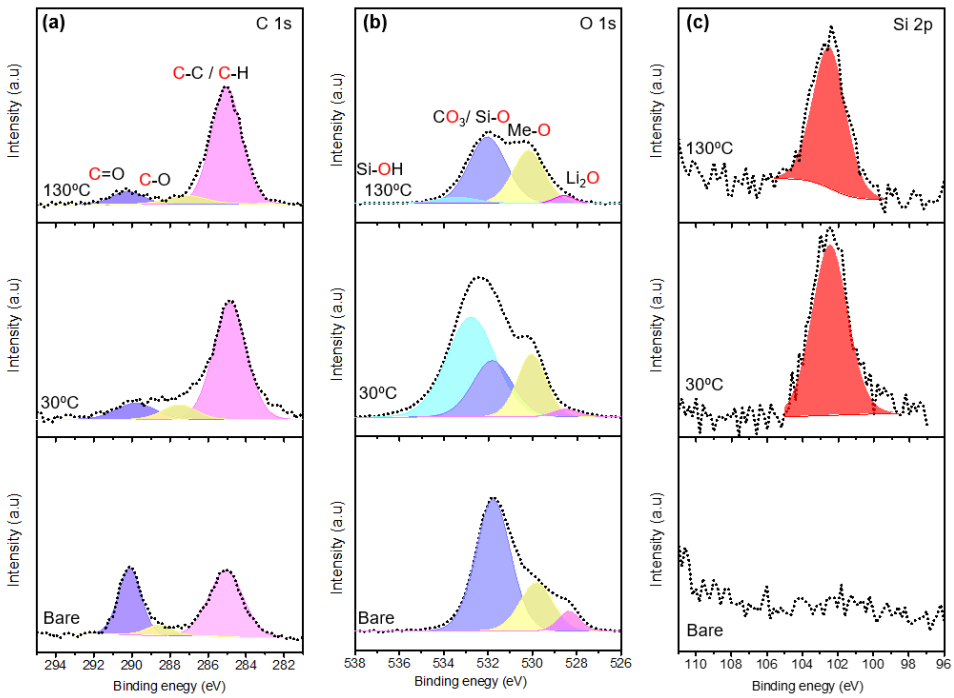

Figure 27. XPS spectra for (a) C 1s (b) O 1s and (c) Si 2p of OTS-NCM82 after (top) and before (middle) heat treatment of 130°C, Bare-NCM82 (bottom). The fitted curves are depicted as colored peaks.

Table 2. The ICP-OES results of Bare and OTS-Ni-rich powder.

	Bare Ni-rich / ppm	OTS-Ni-rich / ppm
Li	88030	84400
Ni	627500	608100
Co	60710	58930
Mn	55530	53810
Si	n/a	n/a

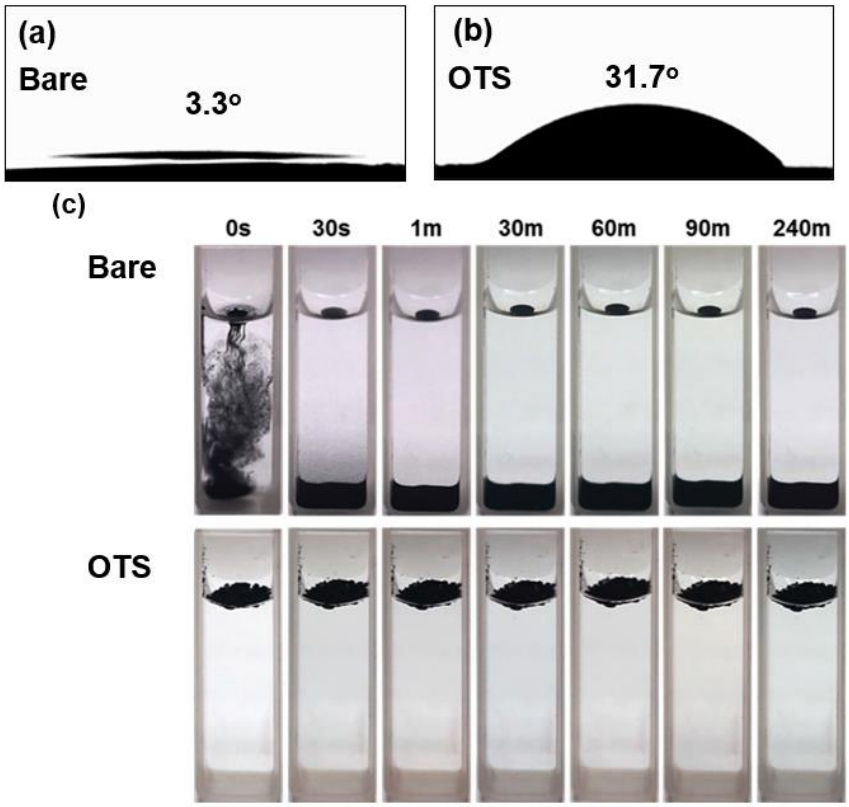

Figure 28. Photos showing the contact angles of the electrolyte droplets on the pellets of (a) Bare-NCM82 and (b) OTS-NCM82. (c) Photos showing the dispersion characteristics vs. time of Bare (top) and OTS-NMC82 (bottom) from the side view of the vials with water.

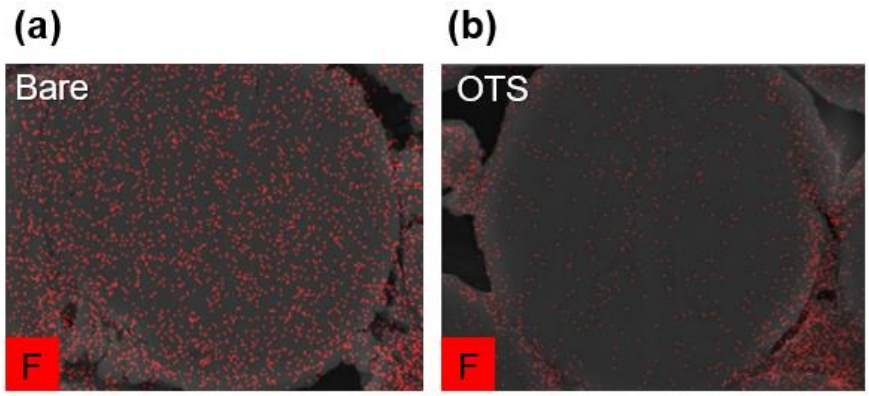

Figure 29. Cross-sectional FE-SEM and F-EDX mapping images of the electrodes of (a) Bare-NCM82 and (b) OTS-NCM82. The electrodes were wetted by 1.0 M $LiPF_6$/EC:DEC (1:1 vol.%) and dried without washing.

4.2.2. Mitigations of microcrack and internal side reaction

Figure 30a exhibits the first voltage profiles of two cells. Compared to the cell with Bare electrode, which had 233.6 and 199.6 mAh g^{-1} of charging and discharge capacity, the cell with OTS electrode had slightly decreased capacities of 225.8 and 186.0 mAh g^{-1} for charging and discharge, respectively. Three redox peaks correlated to phase transition are observed in the calculated dQ dV^{-1} curves in **Figure 30b**. The initial hexagonal structure transforming into a monoclinic is indicated by the peak at 3.7 V vs. Li/Li^{+} during charging. The phase transition from a monoclinic to a second hexagonal structure is reflected in the following peak at 4.0 V. The last peak at 4.15 V represents the change to the third hexagonal phase.[55] In contrast to OTS sample, where the electrolyte/active material interface was only formed on the outer of the secondary particle. The electrolyte on grain boundary of Bare-NCM82 increased the active area for electrochemical reaction, as shown in the EDS mapping results in **Figure 29**.

GITT was performed to compare the Li^{+} ion diffusion of both electrodes, and the results are indicated in **Figure 31a and b**. Although OTS-NCM82 had slightly lower lithium-ion diffusivity than Bare, both materials have comparable diffusivity. In terms of active

interfacial area, because an electrolyte-phobic surface limited the interface, OTS-NCM82 showed slightly larger polarization than the Bare sample, even though it was not considerable. **Figure 31c** exhibits the cyclabilities of the cells with Bare and OTS-NCM82 cathodes. Although the capacity of Bare-NCM82 was 199.2 mAh g^{-1}, which was slightly higher than OTS-NCM82 (186.0 mAh g^{-1}) at first discharge due to the large electrolyte contact area, the capacity of the Bare sample sharply decreases after the 70th cycle. Then it was recorded as 42.6 mAh g^{-1} at the 100th cycle owing to high polarization.[86] On the other hand, this rapid cycling degradation was significantly alleviated in the case of OTS-NCM82, representing a discharge capacity of 136.5 mAh g^{-1} after the 100th cycling. **Figure 32** depicts the voltage profiles and the calculated dQ dV^{-1} curves during cycling. A rapid polarization growth was observed for the Bare sample. In addition to the voltage profile, the steady polarization increase was exhibited in dQ dV^{-1} plot. The peak related to phase transition at 3.6 V for the 1st cycle was steadily polarized to 4.1 V for the 100th cycle. However, the highly repeated voltage curves and maintained dQ dV^{-1} curves was offered from OTS-NCM82. Therefore, these results represent the degradation mode of Bare sample was effectively suppressed by the surface modification from OTS.

Figure 33 shows the voltage profiles obtained under various current densities for rate capability tests. In the cases of the lower current densities than 2C, Bare and OTS-NCM82 have comparable specific discharge capacities. On the other hand, under the high current density over 5C, OTS-NCM82 had the lower discharge capacity compared to Bare. It indicates that the electrolyte-phobic function from OTS is thought to limit the 5 C current density because of the reduced electrolyte accessibility by the decreased interface area.

EIS tests were conducted to analyze the polarization behaviors after the 1st and 70th cycling. Two semicircles were obtained according to the equivalent circuit in the inset of **Figure 34b**. The semicircle in high-frequency region on the left side and the semicircle in high-frequency region on the right side are represent the resistance of surface film and charge transfer resistances, respectively. Also, the ohmic resistance is represented by the intercept on the Z' axis where the semicircle related to film resistance begins. Especially in the case of the 1st cycle, the cell with OTS-NCM82 cathode had a higher total resistance than Bare-NCM82. It is consistent with the high polarization from voltage curves. Interestingly, the ohmic resistance of the Bare-NCM82 significantly increased compared to the 1st charging. The increase in ohmic resistance can be understood as a decrease in ion transport due to contact loss due to microcrack and

electrolyte consumption. To clearly determine the origin of ohmic resistance, the EIS was repeated after replacing a new electrolyte. As a result, the ohmic resistance was partially reduced after refilling the electrolyte. (**Figure 34**) It is believed that the electrolyte is consumed owing to internal side reaction, increasing solution resistance. On the other hand, the ohmic resistance increase was highly mitigated by preventing the electrolyte penetration for OTS-NCM82.

The cells were disassembled after the 50th cycle, and cross-sectional SEM observation was conducted to understand the degradation mechanism. **Figure 35** shows the SEM images of two electrodes after cycling. Interestingly, although it is well known that the mechanical strain from the large c-lattice change during cycling cause the propagation of crack from core to surface along with grain boundaries for the Ni-rich layered oxide, microcrack generation was highly mitigated for OTS-NCM82. It is believed that OTS electrolyte-phobic coating hinders electrolyte penetration into the secondary particle, preventing the internal gas generation from the electrolyte decomposition, which induce severe mechanical stress to the relatedly weak core side. On the other hand, the rough surface passivation, which is thought to be from electrolyte decomposition,[29, 87, 88] on the boundary of primary particle was observed for Bare-

NCM82 as shown in the inset of **Figure 35c**. This thin SEI on the surface of the particle reflects that the initially penetrated electrolyte induces unfavorable side reactions during electrochemical reactions. Therefore, the surface film from the electrolyte decomposition was observed in the core side of the secondary particle. It is reported that electrolyte decomposition usually accompanies gas generation such as CO_2 and O_2.[29, 87, 88] Given that the high Ni composition in transition metal ions facilitates electrolyte decomposition because of the unstable Ni^{4+} ion after charging, these failure modes are more severe in Ni-rich layered oxide than in other cathode materials.

The XPS spectra after the 50th cycle is exhibited in **Figure 36**. It is demonstrated that the intensity of the C-C peak at 285 eV of OTS-NCM82 was higher than that of Bare-NCM82, indicating the surface film from OTS was highly retained after cycling. Electrolyte decomposition could be predicted by increasing the intensities of the peaks of C-O and C=O in C 1s, PO_x in O 1s, PO_yF_z in P 2p, and LiF in F 1s. Based on this, it was observed that OTS effectively mitigates electrolyte decomposition. In addition, a much higher shift of the Ni 2p peak to the low binder energy in Bare-NCM82 than in OTS-NCM82 supports this result.

Figure 37 shows a schematic illustration representing the changes in Bare and OTS-NCM82 particles after wetting with the electrolyte

and cycling. The electrolyte is soaked along with the grain boundaries indicated by the red line for Bare-NCM82. The electrolyte is decomposed on the primary particles with the gas generation during the repeated cycling. This phenomenon induces high pressure inside the particle, accelerating microcracks failure. In contrast, the electrolyte-phobic surface from OTS inhibits the electrolyte penetration into core side. As a result, the particle crack is highly mitigated by preventing the electrolyte wetting. This result demonstrates that the internal side reaction is crucial origin for microcrack, and the electrolyte-phobic coating is effective to relieve the particle cracks.

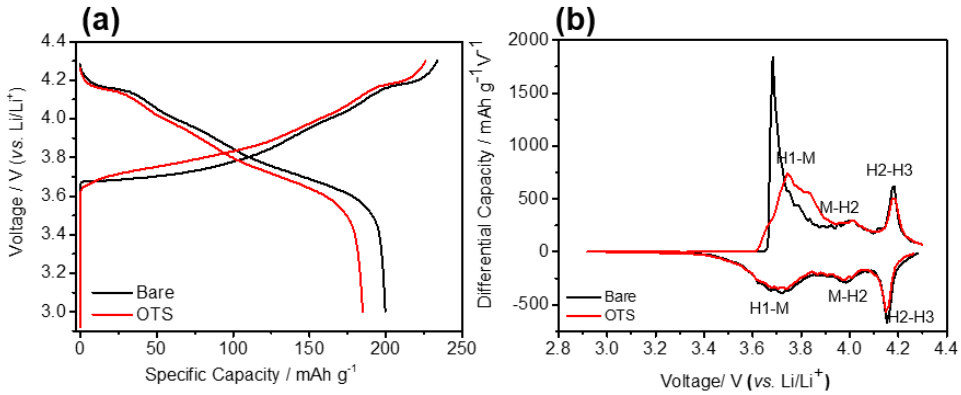

Figure 30. (a) Initial voltage curves from the coin half-cell with Bare-NCM82 and OTS-NCM82. Current density: 40 mA g^{-1}. Voltage cut-off: 4.3 – 3.0 V (vs. Li/Li^+). (b) dQ dV^{-1} curves from the initial voltage curve.

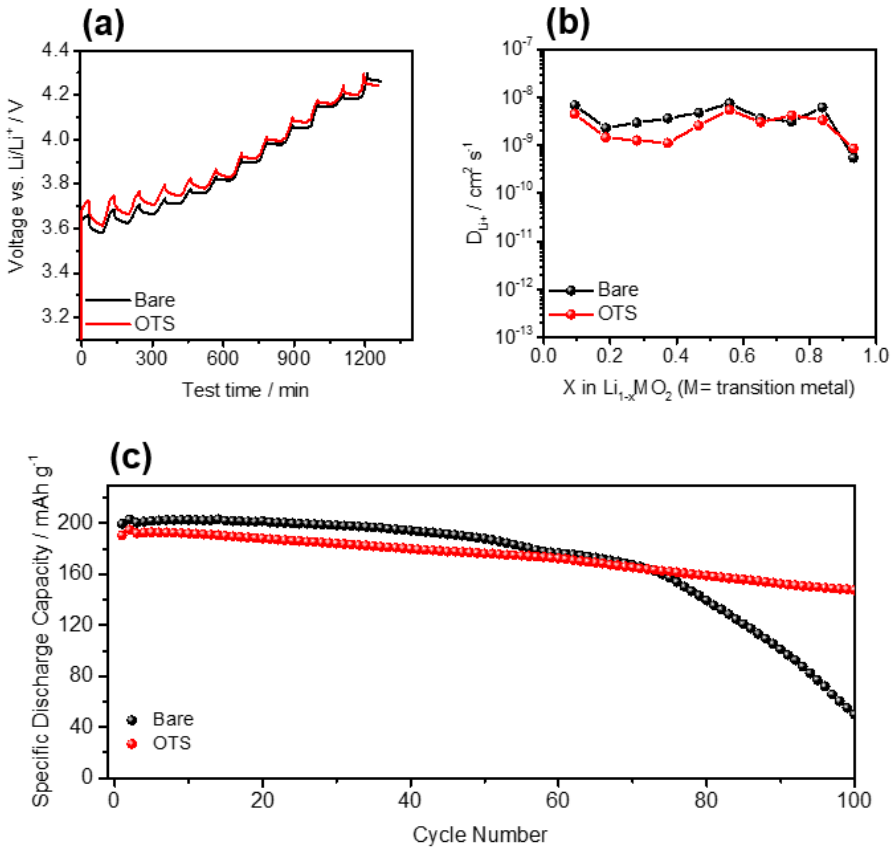

Figure 31. (a) GITT voltage curves and (b)the calculated lithium-ion diffusivities of Bare-NCM82 and OTS-NCM82 cells. (c) cycle performance of the half-cell with Bare-NCM82 and OTS-NCM82.

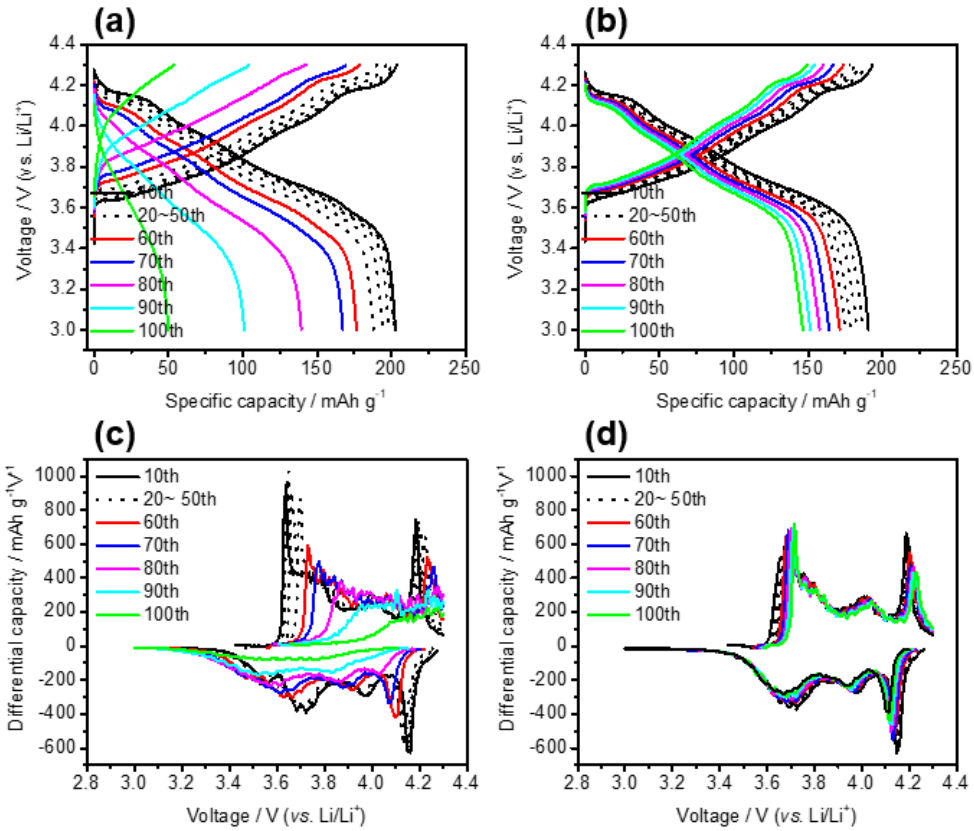

Figure 32. The voltage curves from (a) Bare-NCM82 and (b) OTS-NCM82. The derived dQ dV^{-1} curves for (c) Bare-NCM82 and (d) OTS-NCM82.

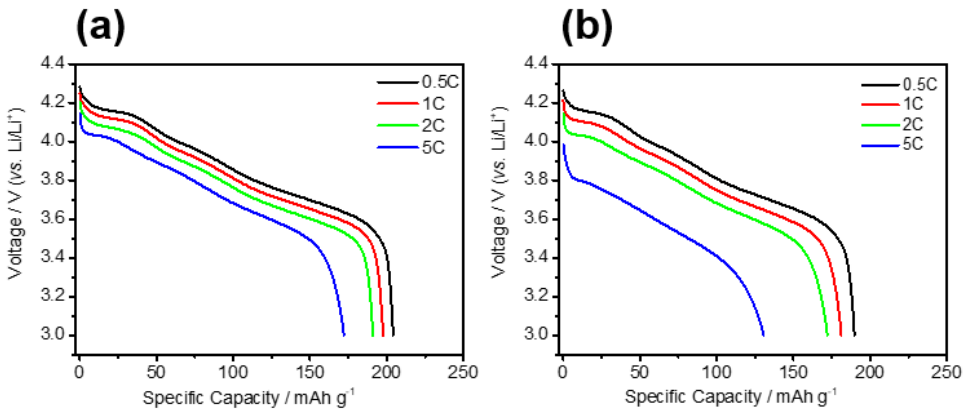

Figure 33. The discharge voltage curves under various current conditions of 0.2, 1, 2, and 5 C for Bare-NCM82 and OTS-NCM82.

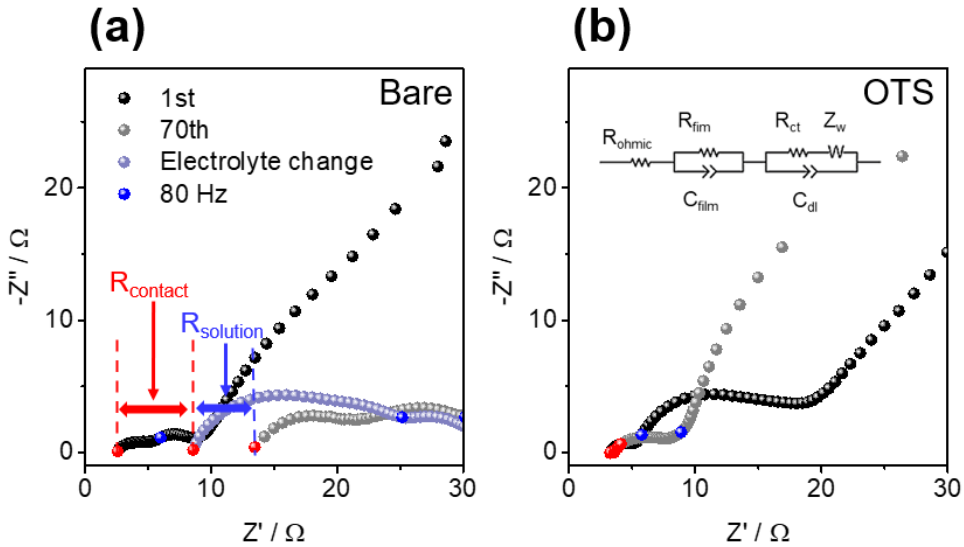

Figure 34. Nyquist plots of the fully charged cells at 4.3 V vs. Li/Li^+ with (a) Bare-NCM82 and (b) OTS-NCM82 after the 1st and 70th cycles.

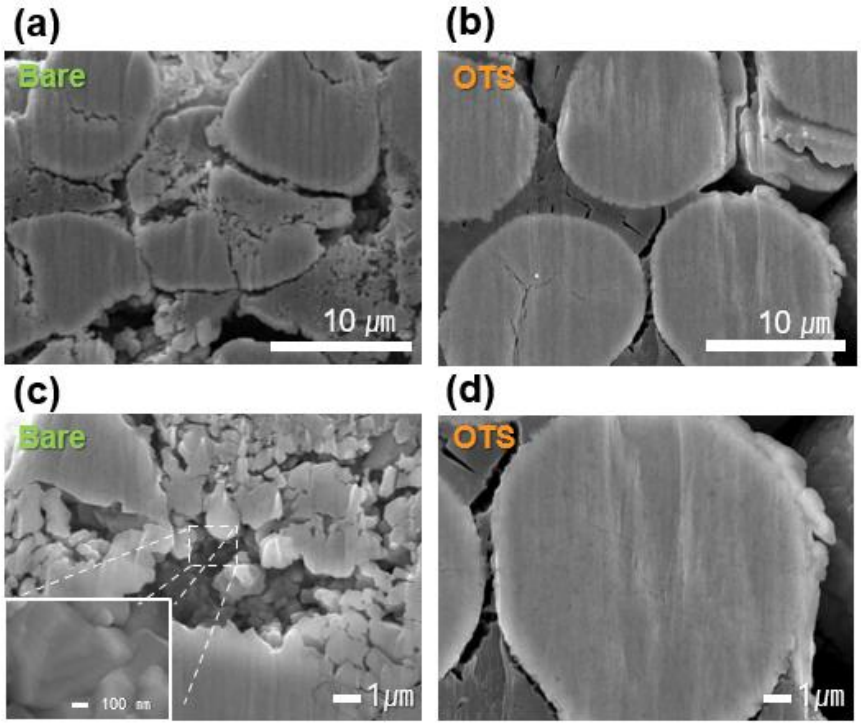

Figure 35. Cross-sectional FE-SEM image of (a and c) Bare-NCM82 and (b and d) OTS-NCM82 after the 50th cycle.

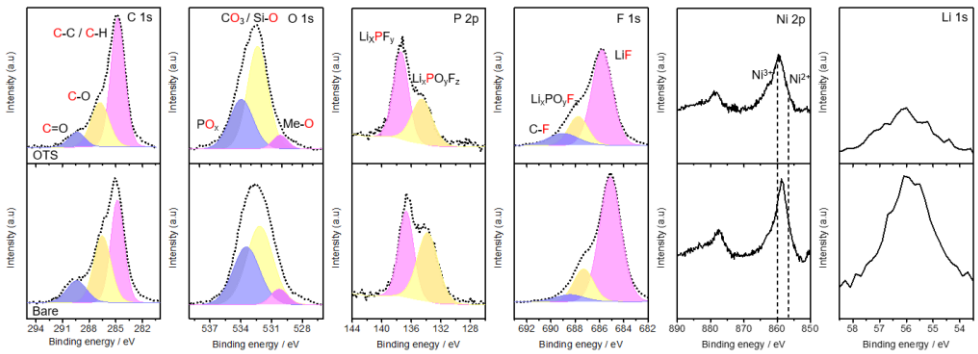

Figure 36. After the 50th cycle, XPS results (C 1s, O 1s, P 2p, F 1s, Ni 2p and Li 1s) of Bare (bottom) and OTS-NCM82 electrode (top). The convoluted peaks are depicted as colored peaks.

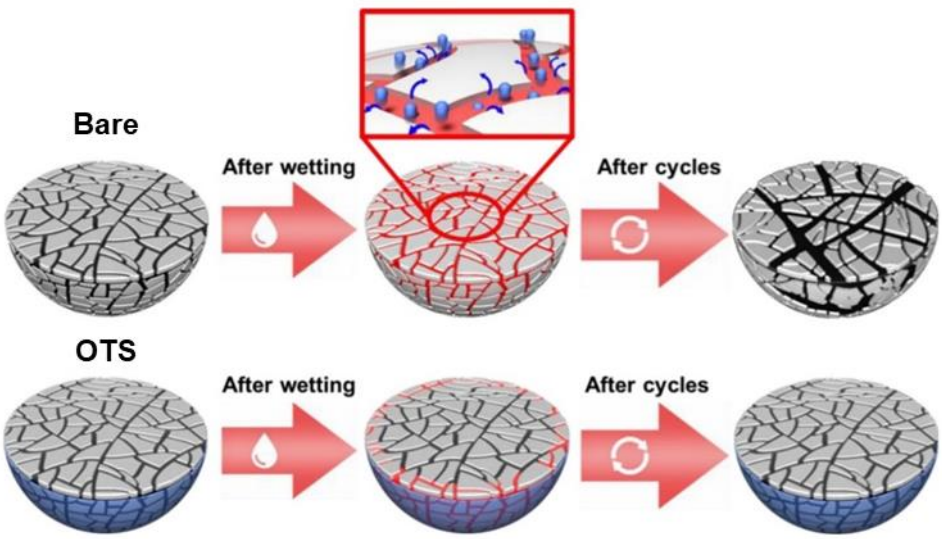

Figure 37. Schematic figures for the microcrack failure mode with Bare-NCM82 (top) and for the microcrack relief by mitigating with OTS-NCM82 (bottom).

5. Conclusion

To remove the residual lithium impurities on the surface, Ni-rich layered oxide was washed with water solvent for 5 or 10 min and heated at 600°C or 800°C. The discharge capacity of Bare sharply decreased from the 60th cycle owing to the attack of fluoric acid formed from the reaction between LiOH and PF_6^- of lithium salt. It was demonstrated the washing effectively mitigated the degradation. However, the capacity retentions until 60th cycles indicated that washing degraded the cycling performance. The origin of the degradation was revealed as NiO like phase generated from the Li^+/H^+ ion exchange during washing. Although the subsequent calcination induces the re-synthesis from the NiO like phase and lithium impurities, the surface state was not recovered to its initial status. Next, Ni-rich layered oxide was modified using a manganese sulfate aqueous solution for 5 min and annealed at 600°C or 800°C. The cathode material coated at low temperatures had similar cyclability to the washed sample. However, because NiO like phase was eliminated by Ni doping in the Li_2MnO_3 coating layer at high temperature, the Ni-rich layered oxide coated at 800°C had improved electrochemical performance.

It was demonstrated that the electrolyte penetrated the secondary particles of Ni-rich layered oxide. The gas phase from the electrolyte decomposition on the grain boundary induces high pressure, accelerating microcracks. The electrolyte-phobic coating was delivered using an OTS of self-assembled monolayer through a vapor deposition process to prevent electrolyte penetration. The surface monolayer from the OTS effectively changes from hydrophilic to hydrophobic, electrolyte-phobic. As a result, the surface layer inhibited the electrolyte soaking along with the grain boundary. Although the reduced electrolyte accessibility from OTS causes a slight polarization increasing during the initial cycle, the capacity retention was dramatically improved. The particle pulverizations were observed for the sample without coating materials after cycling, whereas the particle cracks were highly relieved for OTS-treated cathode material. It is revealed that controlling the internal side reaction is crucial for the suppression of microcracks.

References

1. Lu, L.; Han, X.; Li, J.; Hua, J.; Ouyang, M., *Journal of power sources* 2013, 226, 272−288.
2. Xia, G.; Cao, L.; Bi, G., *Journal of power sources* 2017, 367, 90−105.
3. Lin, X.; Salari, M.; Arava, L. M. R.; Ajayan, P. M.; Grinstaff, M. W., *Chemical Society Reviews* 2016, 45 (21), 5848−5887.
4. Xu, K., Chemical reviews 2014, 114 (23), 11503−11618.
5. Zhang, X. Q.; Cheng, X. B.; Zhang, Q., *Advanced Materials Interfaces 2018*, 5 (2), 1701097.
6. Yulaev, A.; Oleshko, V.; Haney, P.; Liu, J.; Qi, Y.; Talin, A. A.; Leite, M. S.; Kolmakov, A., *Nano Letters* 2018, 18 (3), 1644−1650.
7. Hu, R.; Zhang, H.; Lu, Z.; Liu, J.; Zeng, M.; Yang, L.; Yuan, B.; Zhu, M., *Nano Energy* 2018, 45, 255−265.
8. Qian, J.; Henderson, W. A.; Xu, W.; Bhattacharya, P.; Engelhard, M.; Borodin, O.; Zhang, J.−G., *Nature communications* 2015, 6, 6362.
9. Alvarado, J.; Schroeder, M. A.; Pollard, T. P.; Wang, X.; Lee, J. Z.; Zhang, M.; Wynn, T.; Ding, M.; Borodin, O.; Meng, Y. S., *Energy & Environmental Science* 2019, 12 (2), 780−794.
10. Wu, J.; Cao, Y.; Zhao, H.; Mao, J.; Guo, Z., *Carbon Energy* 2019, 1 (1), 57−76.
11. Teki, R.; Datta, M. K.; Krishnan, R.; Parker, T. C.; Lu, T. M.; Kumta, P. N.; Koratkar, N., *small* 2009, 5 (20), 2236−2242.
12. Chen, Z.; Wang, C.; Lopez, J.; Lu, Z.; Cui, Y.; Bao, Z., *Advanced Energy Materials* 2015, 5 (8), 1401826.
13. Reddy, M. V.; Subba Rao, G.; Chowdari, B., *Chemical reviews* 2013, 113 (7), 5364−5457.
14. Reimers, J. N.; Dahn, J., *Journal of The Electrochemical Society* 1992, 139 (8), 2091−2097.
15. Kim, J.; Kang, H.; Go, N.; Jeong, S.; Yim, T.; Jo, Y. N.; Lee, K. T.; Mun, J., *Journal of Materials Chemistry A* 2017, 5 (47), 24892−24900.
16. Mizushima, K.; Jones, P.; Wiseman, P.; Goodenough, J. B., LixCoO2 ($0< x\leqslant 1$): *Solid State Ionics* 1981, 3, 171−174.
17. Jeong, S.; Kim, J.; Mun, J., *Journal of The Electrochemical Society* 2018, 166 (3), A5038.
18. Noh, H.−J.; Youn, S.; Yoon, C. S.; Sun, Y.−K., *Journal of power sources* 2013, 233, 121−130.
19. Xiong, X.; Wang, Z.; Guo, H.; Zhang, Q.; Li, X., *Journal of Materials*

Chemistry A 2013, 1 (4), 1284–1288.
20. Krüger, S.; Hanisch, C.; Kwade, A.; Winter, M.; Nowak, S., *Journal of Electroanalytical Chemistry* 2014, 726, 91–96.
21. Chen, Z.; Wang, J.; Chao, D.; Baikie, T.; Bai, L.; Chen, S.; Zhao, Y.; Sum, T. C.; Lin, J.; Shen, Z., *Scientific reports* 2016, 6, 25771.
22. Cho, W.; Kim, S.–M.; Song, J. H.; Yim, T.; Woo, S.–G.; Lee, K.–W.; Kim, J.–S.; Kim, Y.–J., *Journal of Power Sources* 2015, 282, 45–50.
23. Liu, W.; Oh, P.; Liu, X.; Lee, M. J.; Cho, W.; Chae, S.; Kim, Y.; Cho, J., *Angewandte Chemie International Edition* 2015, 54 (15), 4440–4457.
24. Zhang, J.; Yang, Z.; Gao, R.; Gu, L.; Hu, Z.; Liu, X., *ACS Applied Materials & Interfaces* 2017, 9 (35), 29794–29803.
25. Zhou, P.; Meng, H.; Zhang, Z.; Chen, C.; Lu, Y.; Cao, J.; Cheng, F.; Chen, J., *Journal of Materials Chemistry A* 2017, 5 (6), 2724–2731.
26. Zhao, W.; Zheng, J.; Zou, L.; Jia, H.; Liu, B.; Wang, H.; Engelhard, M. H.; Wang, C.; Xu, W.; Yang, Y., *Advanced Energy Materials* 2018, 1800297.
27. Muto, S.; Sasano, Y.; Tatsumi, K.; Sasaki, T.; Horibuchi, K.; Takeuchi, Y.; Ukyo, Y., *Journal of The Electrochemical Society* 2009, 156 (5), A371–A377.
28. Sasaki, T.; Nonaka, T.; Oka, H.; Okuda, C.; Itou, Y.; Kondo, Y.; Takeuchi, Y.; Ukyo, Y.; Tatsumi, K.; Muto, S., *Journal of The Electrochemical Society* 2009, 156 (4), A289–A293.
29. Jeong, S.; Kim, K. C.; Lee, S. R.; Mun, J., *Electrochimica Acta* 2019, 300, 156–162.
30. Chen, Z.; Ren, Y.; Jansen, A. N.; Lin, C.–k.; Weng, W.; Amine, K., *Nature communications* 2013, 4, 1513.
31. Xu, M.; Tsiouvaras, N.; Garsuch, A.; Gasteiger, H. A.; Lucht, B. L., *The Journal of Physical Chemistry C* 2014, 118 (14), 7363–7368.
32. Nayak, P. K.; Grinblat, J.; Levi, M.; Aurbach, D., *Journal of The Electrochemical Society* 2015, 162 (4), A596–A602.
33. Liu, L.; Wang, Z.; Li, H.; Chen, L.; Huang, X., *Solid State Ionics* 2002, 152, 341–346.
34. Sun, Y.–K.; Cho, S.–W.; Myung, S.–T.; Amine, K.; Prakash, J., *Electrochimica Acta* 2007, 53 (2), 1013–1019.
35. Wang, J.–H.; Wang, Y.; Guo, Y.–Z.; Ren, Z.–Y.; Liu, C.–W., *Journal of Materials Chemistry A* 2013, 1 (15), 4879–4884.
36. Kim, Y.; Kim, H. S.; Martin, S. W., *Electrochimica Acta* 2006, 52 (3), 1316–1322.
37. Negi, R. S.; Culver, S. P.; Mazilkin, A.; Brezesinski, T.; Elm, M.

T., *ACS Applied Materials & Interfaces* 2020, 12 (28), 31392-31400.
38. Fan, Q.; Lin, K.; Yang, S.; Guan, S.; Chen, J.; Feng, S.; Liu, J.; Liu, L.; Li, J.; Shi, Z., *Journal of Power Sources* 2020, 477, 228745.
39. Lin, F.; Markus, I. M.; Nordlund, D.; Weng, T.-C.; Asta, M. D.; Xin, H. L.; Doeff, M. M., *Nature communications* 2014, 5 (1), 1-9.
40. Bak, S.-M.; Hu, E.; Zhou, Y.; Yu, X.; Senanayake, S. D.; Cho, S.-J.; Kim, K.-B.; Chung, K. Y.; Yang, X.-Q.; Nam, K.-W., *ACS applied materials & interfaces* 2014, 6 (24), 22594-22601.
41. Wang, L.; Maxisch, T.; Ceder, G., *Chemistry of materials* 2007, 19 (3), 543-552.
42. Gu, W.; Dong, Q.; Zheng, L.; Liu, Y.; Mao, Y.; Zhao, Y.; Duan, W.; Lin, H.; Shen, Y.; Chen, L., *ACS Applied Materials & Interfaces* 2019, 12 (1), 1937-1943.
43. Jung, R.; Morasch, R.; Karayaylali, P.; Phillips, K.; Maglia, F.; Stinner, C.; Shao-Horn, Y.; Gasteiger, H. A., *Journal of The Electrochemical Society* 2018, 165 (2), A132-A141.
44. Doo, S. W.; Lee, S.; Kim, H.; Choi, J. H.; Lee, K. T., *ACS Applied Energy Materials* 2019, 2 (9), 6246-6253.
45. Dahn, J.; Fuller, E.; Obrovac, M.; Von Sacken, U., *Solid State Ionics* 1994, 69 (3-4), 265-270.
46. Wang, Y.; Jiang, J.; Dahn, J., *Electrochemistry Communications* 2007, 9 (10), 2534-2540.
47. Ho, V.-C.; Jeong, S.; Yim, T.; Mun, J., *Journal of Power Sources* 2020, 450, 227625.
48. Jung, Y. S.; Cavanagh, A. S.; Dillon, A. C.; Groner, M. D.; George, S. M.; Lee, S.-H., *Journal of The Electrochemical Society* 2010, 157 (1), A75-A81.
49. Ross, G.; Watts, J.; Hill, M.; Morrissey, P., *Polymer* 2000, 41 (5), 1685-1696.
50. Hartmann, L.; Oswald, S.; Graf, M.; Pritzl, D.; Gasteiger, H. A. *ECS Meeting Abstracts*, IOP Publishing: 2020; p 214.
51. Xiong, X.; Wang, Z.; Yue, P.; Guo, H.; Wu, F.; Wang, J.; Li, X., *Journal of Power Sources* 2013, 222, 318-325.
52. Hamam, I.; Zhang, N.; Liu, A.; Johnson, M.; Dahn, J., *Journal of The Electrochemical Society* 2020, 167 (13), 130521.
53. Lu, X.; Li, X.; Wang, Z.; Guo, H.; Yan, G.; Yin, X., *Applied surface science* 2014, 297, 182-187.
54. Xie, H.; Hu, G.; Du, K.; Peng, Z.; Cao, Y., *Journal of Alloys and Compounds* 2016, 666, 84-87.
55. Ryu, H.-H.; Park, K.-J.; Yoon, C. S.; Sun, Y.-K., *Chemistry of Materials* 2018, 30 (3), 1155-1163.

56. Lim, J.-M.; Hwang, T.; Kim, D.; Park, M.-S.; Cho, K.; Cho, M., *Scientific reports* 2017, 7, 39669.
57. Sun, H.-H.; Manthiram, A., *Chemistry of Materials* 2017, 29 (19), 8486-8493.
58. Yan, P.; Zheng, J.; Liu, J.; Wang, B.; Cheng, X.; Zhang, Y.; Sun, X.; Wang, C.; Zhang, J.-G., *Nature Energy* 2018, 3, 600.
59. Xu, G.-L.; Liu, Q.; Lau, K. K.; Liu, Y.; Liu, X.; Gao, H.; Zhou, X.; Zhuang, M.; Ren, Y.; Li, J., *Nature Energy* 2019, 4 (6), 484-494.
60. Kim, H.; Kim, M. G.; Jeong, H. Y.; Nam, H.; Cho, J., *Nano letters* 2015, 15 (3), 2111-2119.
61. Mo, W.; Wang, Z.; Wang, J.; Li, X.; Guo, H.; Peng, W.; Yan, G., *Chemical Engineering Journal* 2020, 400, 125820.
62. Ulman, A., *Chemical reviews* 1996, 96 (4), 1533-1554.
63. Schreiber, F., *Progress in surface science* 2000, 65 (5-8), 151-257.
64. Kobayashi, S.; Nishikawa, T.; Takenobu, T.; Mori, S.; Shimoda, T.; Mitani, T.; Shimotani, H.; Yoshimoto, N.; Ogawa, S.; Iwasa, Y., *Nature materials* 2004, 3 (5), 317-322.
65. Ito, Y.; Virkar, A. A.; Mannsfeld, S.; Oh, J. H.; Toney, M.; Locklin, J.; Bao, Z., *Journal of the American Chemical Society* 2009, 131 (26), 9396-9404.
66. Zheng, G.; Wang, C.; Pei, A.; Lopez, J.; Shi, F.; Chen, Z.; Sendek, A. D.; Lee, H.-W.; Lu, Z.; Schneider, H., *ACS Energy Letters* 2016, 1 (6), 1247-1255.
67. Kim, T. H.; Lee, S. H.; Lee, J.; Song, H. S.; Oh, E. H.; Park, T. H.; Hong, S., *Advanced Materials* 2009, 21 (1), 91-94.
68. Wu, F.; Tian, J.; Su, Y.; Wang, J.; Zhang, C.; Bao, L.; He, T.; Li, J.; Chen, S., *ACS applied materials & interfaces* 2015, 7 (14), 7702-7708.
69. Azmi, R.; Masoumi, M.; Ehrenberg, H.; Trouillet, V.; Bruns, M., *Surface and Interface Analysis* 2018, 50 (11), 1132-1137.
70. Matsunaga, T.; Komatsu, H.; Shimoda, K.; Minato, T.; Yonemura, M.; Kamiyama, T.; Kobayashi, S.; Kato, T.; Hirayama, T.; Ikuhara, Y., *The journal of physical chemistry letters* 2016, 7 (11), 2063-2067.
71. Jarvis, K. A.; Deng, Z.; Allard, L. F.; Manthiram, A.; Ferreira, P. J., *Chemistry of materials* 2011, 23 (16), 3614-3621.
72. Lu, Z.; MacNeil, D.; Dahn, J., *Electrochemical and Solid-State Letters* 2001, 4 (11), A191.
73. Rana, J.; Kloepsch, R.; Li, J.; Scherb, T.; Schumacher, G.; Winter, M.; Banhart, J., *Journal of Materials chemistry A* 2014, 2 (24), 9099-9110.
74. Xiao, R.; Li, H.; Chen, L., *Chemistry of Materials* 2012, 24 (21),

4242−4251.
75. Ye, D.; Sun, C.; Chen, Y.; Ozawa, K.; Hulicova−Jurcakova, D.; Zou, J.; Wang, L., *Nano Research* 2015, 8 (3), 808−820.
76. Kong, F.; Longo, R. C.; Yeon, D.−H.; Yoon, J.; Park, J.−H.; Liang, C.; KC, S.; Zheng, Y.; Doo, S.−G.; Cho, K., *The Journal of Physical Chemistry C* 2015, 119 (38), 21904−21912.
77. Lu, Z.; Beaulieu, L.; Donaberger, R.; Thomas, C.; Dahn, J., *Journal of the electrochemical society* 2002, 149 (6), A778.
78. Kim, Y. S.; Kim, J. H.; Sun, Y.−K.; Yoon, C. S., *ACS Applied Materials & Interfaces* 2022, 14, 17500−17508.
79. Huang, C.; Katz, H. E.; West, J. E., *Langmuir* 2007, 23 (26), 13223−13231.
80. Liu, Y.; Liu, P.; Xiao, Y., *Chinese Science Bulletin* 2012, 57 (15), 1879−1885.
81. Sung, M. M.; Kluth, G. J.; Yauw, O. W.; Maboudian, R., *Langmuir* 1997, 13 (23), 6164−6168.
82. Cohen, S. R.; Naaman, R.; Sagiv, J., *The Journal of Physical Chemistry* 1986, 90 (14), 3054−3056.
83. Britt, D. W.; Hlady, V., *Journal of colloid and interface science* 1996, 178 (2), 775−784.
84. Kluth, G. J.; Sung, M. M.; Maboudian, R., *Langmuir* 1997, 13 (14), 3775−3780.
85. Kluth, G. J.; Sander, M.; Sung, M. M.; Maboudian, R., *Journal of Vacuum Science & Technology A: Vacuum, Surfaces, and Films* 1998, 16 (3), 932−936.
86. Yang, W.; Xiang, W.; Chen, Y.−X.; Wu, Z.−G.; Hua, W.−B.; Qiu, L.; He, F.−R.; Zhang, J.; Zhong, B.−H.; Guo, X.−D., *ACS applied materials & interfaces* 2020, 12 (9), 10240−10251.
87. Mun, J.; Yim, T.; Park, K.; Ryu, J. H.; Kim, Y. G.; Oh, S. M., *Journal of The Electrochemical Society* 2010, 158 (5), A453.
88. Liu, T.; Garsuch, A.; Chesneau, F.; Lucht, B. L., *Journal of Power Sources* 2014, 269, 920−926.
89. Jung, R.; Metzger, M.; Maglia, F.; Stinner, C.; Gasteiger, H. A., *Journal of The Electrochemical Society* 2017, 164 (7), A1361.
90. Jo, C.−H.; Cho, D.−H.; Noh, H.−J.; Yashiro, H.; Sun, Y.−K.; Myung, S. T., *Nano Research* 2015, 8 (5), 1464−1479.

국문 초록

리튬이온 전지용 고-니켈계 층상형 양극재의 퇴화 거동 기반 맞춤형 계면 개질

정 성 훈

서울대학교 대학원

화학생물공학부

$LiNi_xCo_yMn_zO_2$ (x > 0.8, x+y+z = 1)의 화학식을 갖는 고-니켈계 층상형 양극재는 저렴한 비용과 고용량 때문에 고에너지 밀도 리튬 이온 배터리 용 양극재로 주목 받고 있다. 그러나 높은 에너지 밀도와 저렴한 가격으로 인한 장점에도 불구하고 고-니켈계 층상형 양극재를 상용화에는 여러 어려움이 있다. 먼저, 표면이 불안정하며 표면에 LiOH와 Li_2CO_3와 같은 잔존 리튬 불순물을 불순물은 갖으며 불안정한 표면은 물과 만나면 리튬 불순물을 증가시킨다. 고-니켈계 층상형 양극재의 경우, 충전 과정에서 니켈 이온이 불안정한 +4로 산화되며, 산소 분자의 방출과 함께 안정한 암염 구조로 변화한다. 이때, 전해질은 이러한 변화에 필요한 전자를 제공함으로써 더욱 산화 분해되기 때문에 퇴화는 표면에서 심각하다. 표면의 부반응을 억제하기 위해서 다양한 표면 개질법이 고안되었다. 또한, 표면의 잔류 불순물의 경우, 충전과정에서 분해되어 가스를 발생시켜 전지의 스웰링 현상을 일으키며 바인더인 Polyvinylidene fluoride (PVdF)의 젤화 시켜 불균일한 전극 제조를 초

래한다. 불순물의 제거함과 동시에 표면의 안정성을 높일 수 있는 방법으로 물을 이용한 표면 개질법이 있으나, 세척 과정은 고-니켈계 층상형 양극재의 수명 퇴화를 유도한다. 다음으로, 고-니켈계 층상형 양극재는 충전 과정 동안 큰 비 등방성 부피 변화를 겪는데, 이로 인해 입자 내 미세 균열이 발생한다. 일차 입자의 표면 개질이 미세균열을 완화한다는 점에서 내부 부반응은 중요한 문제이다.

본 연구에서는, 세척 및 이후 건조 과정에서 리튬 이온과 수소 이온의 교환 및 NiO 유사 상의 생성을 확인하였다. 이렇게 생성된 NiO 유사 상은 고-니켈계 층상형 양극재의 수명 특성을 약화시킨다. NiO 유사 상의 제거를 위해서 Li_2MnO_3로 계면 개질이 수행되었다. 800도의 고온 소성 과정에서 Ni 이온이 Li_2MnO_3 표면층으로 도핑 되는 것을 발견하였고 이는 리튬의 산화 환원 전압 대비 4.65 V의 전압에서 발생하는 산화 반응으로 확인되었다. Ni 도핑 된 Li_2MnO_3 표면층은 수용액을 이용한 코팅 과정에서 발생하는 NiO 유사상을 소모하고 표면을 안정시키는데 효과적이다. 그 결과, Ni 도핑 된 Li_2MnO_3를 포함하는 양극 재료는 0.2C의 전류 밀도와 비교하여 5C의 전류 밀도에서 76.9%의 높은 비율 방전 용량을 보이며, 100번째 사이클에서 88.3%의 용량 유지율을 보였다.

또한, 전해질의 이차 입자로 침투를 방지하여 입자 내부에서의 전해액 부반응을 억제하기 위해 자기 조립 단분자 층(Self-Assembled Molecular Monolayer, SAM) 중 하나인 OTS(octyltrichlorosilane)를 사용하여 전해질과의 친화도를 감소시키는 코팅이 이루어졌다. SAM의 자가 종결 반응 특성으로 인해 고-니켈계 층상형 양극재의 표면에 균질

한 단일 층이 형성된다. 전해질을 배척하는 특성은 입자 내부에서의 전해질 분해로 인한 기체 상 발생을 감소시켜 미세 균열의 형성을 완화하는 데 효과적임이 검증되었다.

키워드 : 리튬 이온 이차전지, 고-니켈계 층상형 양극재, 계면 개질, 자가 조립 단분자층, 세척, 미세 균열

학번 : 2019-34401